

Dynamic and kinematic characterization of the impulsive wavemaker system in a numerical wave tank

Cite as: AIP Advances 10, 115306 (2020); <https://doi.org/10.1063/5.0017376>

Submitted: 22 July 2020 . Accepted: 01 October 2020 . Published Online: 05 November 2020

 C. Barraud, and  R. H. Hernández

COLLECTIONS

Paper published as part of the special topic on [Chemical Physics](#), [Energy, Fluids and Plasmas](#), [Materials Science](#) and [Mathematical Physics](#)



View Online



Export Citation



CrossMark

ARTICLES YOU MAY BE INTERESTED IN

[Riccati transfer matrix method for linear multibody systems with closed loops](#)


AIP Advances 10, 115307 (2020); <https://doi.org/10.1063/5.0029057>

[Magnetostatic determination of variations of internal stress in magnetic steels](#)

AIP Advances 10, 115302 (2020); <https://doi.org/10.1063/5.0004448>

[Deagglomeration of nanoparticle clusters in a “cavitation on chip” device](#)

AIP Advances 10, 115204 (2020); <https://doi.org/10.1063/5.0029070>



Call For Papers!

AIP Advances

SPECIAL TOPIC: Advances in
Low Dimensional and 2D Materials

Dynamic and kinematic characterization of the impulsive wavemaker system in a numerical wave tank

Cite as: AIP Advances 10, 115306 (2020); doi: 10.1063/5.0017376

Submitted: 22 July 2020 • Accepted: 1 October 2020 •

Published Online: 5 November 2020



View Online



Export Citation



CrossMark

C. Barraud  and R. H. Hernández^{a)} 

AFFILIATIONS

LEAF-NL, Departamento de Ingeniería Mecánica, Universidad de Chile, Casilla 2777, Santiago, Chile

^{a)} Author to whom correspondence should be addressed: rohernan@ing.uchile.cl. URL: <https://www.leafnl.uchile.cl>

ABSTRACT

We study the dynamical response of a piston-type wavemaker in a numerical wave tank. The two-dimensional, fully viscous unsteady Navier–Stokes equations are solved on a two-phase flow configuration using the volume of fluid method to capture the free surface dynamics. The wavemaker is a moving wall driven by an arbitrary signal waveform. The step response of the wavemaker may generate pulse-like waves similar to an undular bore propagating along the tank. Wave elevation at the piston wall has close similarity to the time response of second order systems found in feedback theory. The scaling found for water elevation at the piston wall for different step velocities and mean still water levels is in agreement with that in the available theory at low Froude numbers. The results along the tank for continuous waves agree with those of potential theory. The power input during the step response was determined during the whole wave generation process showing that net piston forces are predominantly hydrostatic. A power scaling for different mean still water levels and step velocities as a function of the Froude number was obtained. An active absorption strategy based upon a feedback controller driving a secondary piston was implemented. Wave absorption was successfully achieved on regular and irregular waves.

© 2020 Author(s). All article content, except where otherwise noted, is licensed under a Creative Commons Attribution (CC BY) license (<http://creativecommons.org/licenses/by/4.0/>). <https://doi.org/10.1063/5.0017376>

I. INTRODUCTION

Wave tanks are centerpieces when it comes to studying hydrodynamics and wave structure interaction in offshore and marine engineering. Experimental or numerical, they can reproduce the offshore environmental conditions (waves, currents, winds for some of them) in order to evaluate the dynamic response to these harsh conditions of vessels, offshore platforms, and marine renewable energy structures such as fixed/floating offshore windmills or wave energy converters. For a long time, these phenomena could only be experimentally studied. The wave tank scaling should be done, according to the similarity principle of dimensional analysis, by matching relevant numbers as the Froude and the Reynolds numbers. This is often complicated especially at small scale as explained in Ref. 1. One approach is to test the model through increasing model scales.² The most simple configuration for a wave tank is a 2D tank, which is a long tank where waves are generated on one side and absorbed or broken up on the opposite side.

In order to generate waves at a laboratory scale, one should displace a certain amount of water by means of a wavemaker of choice: piston, hinged paddle, double articulated paddle, plunger, duck. First order wavemaker theory has first been studied in Ref. 3. Wave generation alternatives have been theoretically studied in the 1950s⁴ including piston, hinged paddle, or double articulated paddle. In this work, we choose to use a piston wavemaker where the piston stroke along the tank is the physical mechanism to create waves. The resulting waves from a piston wavemaker were investigated in Ref. 4 determining a transfer function or relationship between the piston stroke and the wave height. A validation of the piston wavemaker theory was provided by some experiments.⁵ Similarly, Madsen⁶ developed a theory of wavemaker generation for pistons providing a detailed expression for wave elevation at any position in a wave tank, and Schäffer⁷ developed the second-order wavemaker theory for irregular waves. Goring⁸ studied solitary wave generation with a piston wavemaker, basing his solution on the theory of Ref. 9. The impulsive wavemaker was experimentally and numerically

studied in Ref. 10, notably showing wave profiles from the experiment as well as forces on the wavemaker.

Most of the research on wavemaker theory has been conducted on the basis of potential theory avoiding the determination of viscous effects. At the same time, the necessity for local solutions at the piston wavemaker was considered important in order to understand the physics of the first instants in the wave generation. Local solutions near the piston wall are provided by Joo *et al.*¹¹ using the Laplace equation and expansion series for small Froude numbers and basing their work on Ref. 12. They investigated the contact line motion at initial times of the piston wavemaker for ramp, step, exponential, and harmonic velocities. They later on extended their studies to stratified fluid.¹³ A study of the steady motion of a ship bow at high Froude number, which is similar to the piston wavemaker problem, was carried out in Ref. 14. Experimental realization of the velocity step case becomes complicated because imposing a prescribed step-like wavemaker motion involves high piston accelerations and therefore peak power inputs. The practical case is to perform a ramp motion as indicated in Ref. 15.

While experimental wave tanks provide a physical platform to implement such systems, testing may be expensive or not suitable to comply with similarity restrictions, whereas numerical studies once performed exclusively with potential codes (irrotational, incompressible, and nonviscous flows) are now commonly carried out taking into account viscous effects that, nevertheless, require more computational resources.

At present, the use of efficient codes solving viscous Navier–Stokes equations has been reported to be useful in order to model extreme wave conditions where the wave breaking process¹⁶ can be captured and identified as the dominant mechanism (instabilities) involved in extreme loading on marine structures and wave energy converter devices.¹⁷ Numerical wave tanks may recreate realistic waves using moving boundaries (which involves a dynamic mesh) or static boundaries with mathematical implementation (in the domain or at the boundaries). In this work, we use the first option that mimics a viscous piston motion in a physical experiment.^{18,19} Most of the numerical wave tank models include the volume of fluid (VOF) to simulate two-phase flows²⁰ as well as the wave generation and propagation problem.^{21–24} Wave tank modeling with active wave absorption was developed in OpenFOAM,^{18,25} and recent methods such as Smoothed-Particle Hydrodynamics (SPH) have also been developed to represent two-phase flows.^{26,27}

In this work, we present a numerical study of a piston wavemaker at a laboratory scale to investigate the wave generation process and characterize the piston wavemaker dynamics, extending Froude number regimes far beyond the ones that were studied before. We perform fully non-linear and viscous numerical simulations of the wave tank where surface waves are produced by

the prescribed motion of a piston wavemaker. The moving boundaries allow reproducing the physics of a real facility. A complete mesh independence study is carried out, and validation is performed with theoretical data. To be able to generate waves of high quality, it is necessary to characterize the wavemaker system. It is chosen here to do so by basing the study on the initial-value problem, theoretically studied in Ref. 11. The numerical simulation allows us to study regimes that do not appear in the theoretical study based on potential flow. We measure the water height at the wavemaker and in the tank for a set of prescribed wavemaker motions, allowing one to characterize the near and far field generated waves and determine the power input needs according to the wavemaker dynamics.

The structure of this article is as follows: the initial-value problem and the required equations are presented in Sec. II, the numerical method, mesh independence tests, and validation are presented in Sec. II C, and finally the resulting characterization of the piston wavemaker and the power input analysis are presented in Sec. III.

II. PROBLEM FORMULATION

The problem is described in the schematics in Fig. 1. We consider a 2D wave tank of length L and height d , equipped with a moving piston wavemaker placed at the left wall, and the opposite wall of the tank is situated on the right. The mean still water level is denoted h and can be varied at will. The origin of the coordinate system is located at the left bottom of the wave tank, and all different measurement stations along the wave tank are referred to this coordinate system. In order to characterize the piston wavemaker and the wave tank behavior, a series of tests will be performed to provide the system response to input velocity signals driving the motion of the piston wavemaker. The overall wave tank response will be obtained from Heaviside $\Theta(t)$ input signals representing a step response test.²⁸ We consider the system composed by the wavemaker, whose input signal is its velocity U_G and the response is the water level at the piston wavemaker η_w , as shown in Fig. 1. We can define a transfer function associated with the wavemaker system, hereafter called G where the fundamental output/input relationship (transfer function) can be expressed as $G = \eta_w/U_G$, which is crucial when implementing feedback controlled wave-absorbers.²⁹

A. Governing equations

The numerical simulation solves the 2D two-phase laminar Navier–Stokes equations with two incompressible fluids (water and air phases). The mass conservation equation is also solved in primitive variables incorporating the VOF model to deal with each fluid phase.²⁰ These equations can be written in the vector form as

$$\nabla \cdot \mathbf{U} = 0, \quad (1)$$

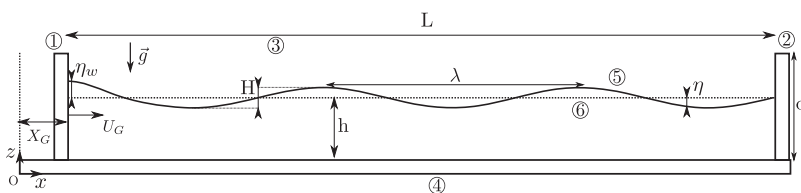


FIG. 1. Schematics of the problem. The numerical domain is composed of (1) the piston wavemaker, (2) the tank end boundary, (3) the atmosphere, and (4) the seabed. The generated waves (5) at the free-water surface are measured with respect to the mean still water level (6) h .

$$\frac{\partial(\rho\mathbf{U})}{\partial t} + \nabla \cdot (\rho\mathbf{U}\mathbf{U}) - \nabla \cdot (\mu\nabla\mathbf{U}) - \nabla\mathbf{U} \cdot \nabla\mu = -\nabla p^* - \mathbf{g} \cdot \mathbf{x}\nabla\rho + \sigma\kappa\nabla\alpha, \tag{2}$$

$$\frac{\partial\alpha}{\partial t} + (\nabla \cdot \mathbf{U})\alpha = 0, \tag{3}$$

where \mathbf{U} is the velocity vector, p^* is the pseudo-dynamic pressure ($p^* = p - \rho\mathbf{g} \cdot \mathbf{x}$), ρ is the density, μ is the dynamic viscosity, \mathbf{g} is the gravity acceleration, \mathbf{x} is the position vector, and σ is the fluid surface tension coefficient. The volume fraction α is introduced to deal with the two-phase formulation within the volume of fluid (VOF) framework. κ is defined as follows:

$$\kappa = -\nabla \cdot \frac{\nabla\alpha}{|\nabla\alpha|}. \tag{4}$$

In the two-phase formulation, density and viscosity on each domain cell are computed as a weighted mean of the form^{30,31}

$$\rho = \alpha\rho_{water} + (1 - \alpha)\rho_{air}, \tag{5}$$

$$\mu = \alpha\mu_{water} + (1 - \alpha)\mu_{air}. \tag{6}$$

The relevant dimensionless number in this work is the Froude number $Fr = U_G/\sqrt{gh}$ controlling the wave propagation dynamics. Viscous effects become important during the interaction of the starting wave with the piston wavemaker taking place at

the beginning of the wave generation as we will discuss in Sec. III C.

B. Boundary conditions

Boundary conditions employed in this work are summarized in Eq. (7). On the piston wavemaker wall, we impose no-slip condition for all velocity components. The initial still water level h is always established before any wavemaker motion by initializing α . The volume fraction α is bounded and may adopt any value within $0 \leq \alpha \leq 1$ in any place of the physical domain, and Neumann boundary conditions, set to 0, are applied at all boundaries for the α variable as well. In particular, at the wavemaker, such a condition forces the contact angle of the interface to be perpendicular to the wavemaker wall, which agrees with the experimental results of Refs. 15 and 32 for the case of a continuously accelerated wavemaker. In this work, the piston wavemaker moves according to an input velocity signal displayed in Fig. 3(a). A velocity step U_G drives the piston resulting in linear dependency on time displacement $X_G(t)$. At the piston wavemaker wall, the velocity matches the velocity of the moving boundary in the x -direction only. A no-slip condition is used at the seabed wall and the right end wall. The pressure is set to a reference pressure (in this case 0) at the atmosphere boundary, and 0-Neumann conditions are used at the other locations. A zero-gradient condition is applied at the atmosphere for outflow, and a velocity u_ϕ is assigned for inflow based on the flux in the patch-normal direction. The boundary conditions for the velocity, pressure, and α variables can be summarized as

$$\left\{ \begin{array}{l} x = X_G(t) \rightarrow u_x = U_G(t), \\ x = L \rightarrow u_x = 0, \\ z = 0 \rightarrow u_x = 0, \\ z = d \rightarrow \begin{array}{l} \text{inflow: } u_x = 0, \\ \text{outflow: } \frac{\partial u_x}{\partial z} = 0, \end{array} \end{array} \right. \quad \begin{array}{l} u_z = 0, \\ u_z = 0, \\ u_z = 0, \\ u_z = u_\phi, \\ \frac{\partial u_z}{\partial z} = 0, \end{array} \quad \begin{array}{l} \frac{\partial p^*}{\partial x} = 0, \\ \frac{\partial p^*}{\partial x} = 0, \\ \frac{\partial p^*}{\partial z} = 0, \\ p^* + \frac{1}{2}|\mathbf{u}|^2 = 0, \end{array} \quad \begin{array}{l} \frac{\partial \alpha}{\partial x} = 0, \\ \frac{\partial \alpha}{\partial x} = 0, \\ \frac{\partial \alpha}{\partial z} = 0, \\ \frac{\partial \alpha}{\partial z} = 0. \end{array} \tag{7}$$

C. Numerical method

The governing equations were solved with the open-source software *OpenFOAM* version 5.³³ *OpenFOAM* is an object oriented C++ toolbox for solving continuum mechanics problems with the finite volume method. *OpenFOAM* presents many advantages: as released under the GNU General Public License, it is free and open-source (no licensing fees, unlimited number of jobs, users, and cores). It is also largely used in the scientific community and thus has been validated for many applications. We use *interDyM-Foam*, a solver of the Navier–Stokes equations for two incompressible isothermal immiscible phases using the volume of fluid (VOF) method. It increases the capabilities of previous solvers allowing one to handle dynamic mesh motion. *OpenFOAM* solves a single equation of momentum for the two-phase mixture by introducing a volume fraction advection equation of the VOF method used to capture the interface between the phases. Hirt and Nichols²⁰ presented this

method as an efficient and simple way of treating the free surface in numerical simulations, as it stores a minimum amount of information. This method should be carefully used when the surface tension becomes important. Some numerical solvers such as *interDyM-Foam* impose some restrictions in order to keep a sharp interface between both fluid phases. An additional term called artificial compression is introduced here,³¹

$$\frac{\partial\alpha}{\partial t} + \nabla \cdot (\alpha\mathbf{U}) + \nabla \cdot (\mathbf{U}_c\alpha(1 - \alpha)) = 0, \tag{8}$$

$$U_c = \min(C_\alpha|\mathbf{U}|, \max(|\mathbf{U}|)). \tag{9}$$

C_α is a user defined coefficient whose default value is 1. The additional term is only active close to the interface because of the product $\alpha(1 - \alpha)$ and does not impact the solution outside the interface

region. Its role is to compress the interface and maintain α between 0 and 1 if used with discretization techniques. In the post-processing stage, the value of $\alpha = 0.5$ is chosen to detect the free surface, which is carried out thanks to linear interpolation. The *interDyMFoam* solver uses the PIMPLE algorithm, which combines both SIMPLE (Semi-Implicit Method for Pressure Linked Equations)³⁴ and PISO (Pressure Implicit Split Operator)³⁵ algorithms and allows for bigger time steps. Simulations were performed on a CPU Xeon E5-2660 v2 cluster running on Simple Linux Utility for Resource Management (Slurm) and based on MPI libraries. The CPU run time for a one second transient simulation and a typical wave was about 2.4 h for a 400 000 element mesh and $\Delta t = 5 \times 10^{-4}$ s time step. The geometry of the wave tank required a fine spatial discretization, particularly in zones such as the water–air interface and zones of high velocity gradients such as the wavemaker walls. Explicit schemes are used so that special care is taken when choosing the time step regarding the mesh size and CFL condition below 1. As a result of the rapid input velocity signals during the wave formation and subsequent progression along the wave tank, the temporal discretization requires time steps smaller than 10^{-3} s; thus, we choose a time step size $\Delta t = 5 \times 10^{-4}$ s for all the simulations.

D. Mesh independence tests

A series of mesh tests are performed to look for mesh independent results. We consider two test cases in order to achieve mesh convergence: (i) the study of the response to an input velocity step characterized by the overshoot and the steady state water height, and the rising, peak, and settling times, as found on the time response of linear dynamical systems, and (ii) the wave propagation of linear waves along the 2D wave tank (wave height, wavelength). In the first case, a set of uniform rectangular cell meshes are generated to look for mesh independence. Most sophisticated meshes, with a uniform zone at the water–air interface, which includes the minimum and the maximum water height during the whole simulation, are also set up. They include refinement at the wavemakers and are denominated “non-uniform.” They allow decreasing the computation time as the mesh size is kept in reasonable limits. The mesh, generated thanks to the *blockMesh* program, is built from three characteristic elements: the cell width at the piston wall Δx_w , the cell

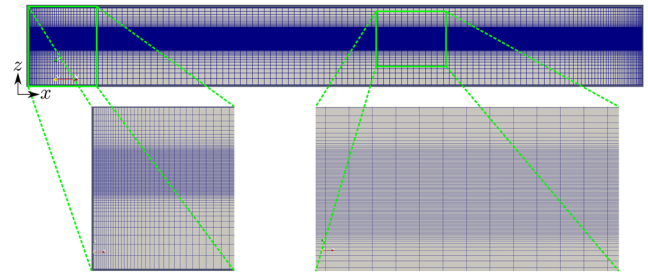


FIG. 2. Non-uniform mesh overview and zoom at the wavemaker and water–air interface. In this case, the wave tank dimensions are 2 m × 0.25 m and water depth is 0.15 m.

width in the wave propagation zone (far from the walls) Δx , and the cell height in the wave propagation zone Δz . Δx_w will be determined from the uniform mesh study in (i). From the wavemaker, the longitudinal element size Δx_i is being computed with the following geometric law: $\Delta x_i = \Delta x_w r^{(i-1)} \forall i < n_j$, where r is the geometric growth rate. After n_j cells, the elements reach a constant size Δx in the wave propagation zone. A similar calculation allows us to define the vertical element size from outside the interface zone. Both Δx and Δz are set up considering the number of cells per wavelength and cells per wave height, respectively. These parameters will be set in (ii). **Figure 2** shows the mesh in the x – z plane, while one cell size is set up in the y -direction. Mesh type and properties are displayed in **Table I**. These preliminary tests with different meshes allow an appropriate choice of the mesh size without compromising accuracy and CPU time (cf. **Fig. 2**). The dynamic mesh is modeled using a mesh expansion/contraction strategy. The mesh uniformly contracts and expands, conserving the global mesh cell volumes as these motions are relatively small compared to the tank length.

1. Step response

In order to fully test the capacity of the code to represent sudden and rapid water surface elevation, we choose to perform a step response of the water tank. The input signal is a velocity step, as

TABLE I. Mesh properties to study the wavemaker response to a velocity step. Δx_w is the cell size in the x -direction at the piston wavemaker, Δx is the cell size in the x -direction in the wave propagation zone, Δz is the cell size in the z -direction at the water–air interface, η_o is the overshoot water height at the piston wavemaker, η_{ss} is its steady state value, and t_r , t_p , t_s are the rising time, the peak time, and the settling time, respectively. The area a is used as an entry for the GCI study.³⁶

		Δx_w (m)	Δx (m)	Δz (m)	a (m^2)	Number of cells	η_o (m)	η_{ss} (m)	t_r (s)	t_p (s)	t_s (s)
Uniform	M_U^1	0.0100	0.0100	0.005 0	5×10^{-5}	10 000	0.0356	0.0257	0.0536	0.1253	0.2819
	M_U^2	0.0050	0.0050	0.002 5	1.25×10^{-5}	40 000	0.0342	0.0257	0.0481	0.1116	0.2979
	M_U^3	0.0025	0.0025	0.001 0	2.5×10^{-6}	200 000	0.0340	0.0259	0.0479	0.1298	0.2905
	M_U^4	0.0015	0.0015	0.000 75	1.125×10^{-6}	443 889	0.0340	0.0258	0.0491	0.1237	0.2939
	M_U^5	0.0013	0.0013	0.000 5	6.5×10^{-7}	769 000	0.0341	0.0259	0.0493	0.1246	0.2927
	M_U^6	0.0011	0.0011	0.000 26	2.9×10^{-7}	1 748 916	0.0341	0.0259	0.0494	0.1247	0.2909
Non-uniform	M_{NU}^7	0.0010	0.0363	0.001 0	...	17 115	0.0340	0.0258	0.0491	0.1264	0.2976
	M_{NU}^8	0.0010	0.0181	0.001 0	...	20 055	0.0340	0.0258	0.0492	0.1262	0.2965
	M_{NU}^9	0.0010	0.0091	0.000 57	...	47 025	0.0341	0.0258	0.0488	0.1250	0.2954

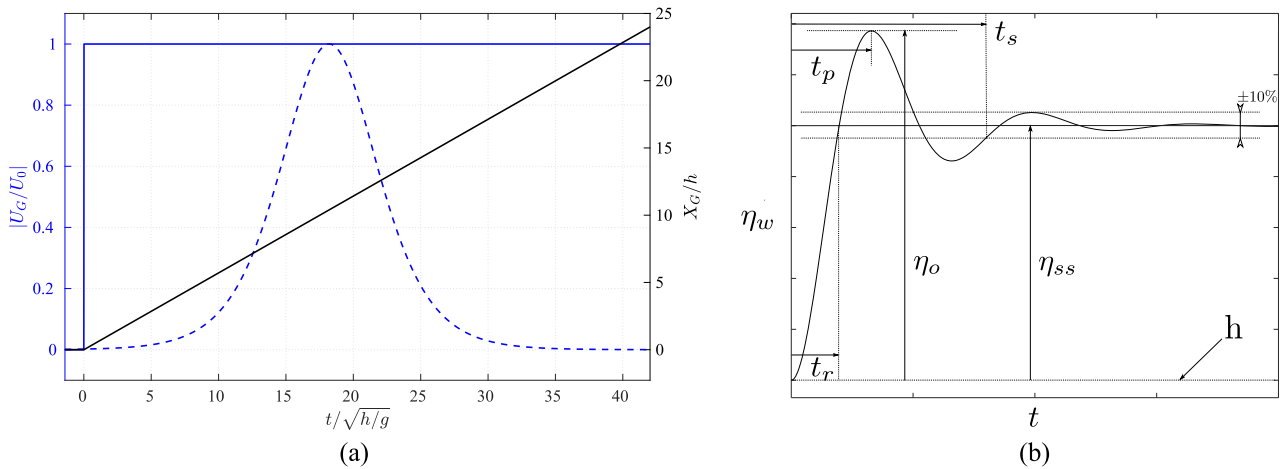


FIG. 3. (a) Normalized input signal for the step response test as a function of non-dimensional time (continuous blue line). The piston velocity $U_G(t)$ is normalized by its maximum value U_0 . We also display the piston position X_G normalized by the water depth of the wave tank (continuous black line). The smooth function for the wave train generation in Sec. III D is also shown (by the dashed blue line). (b) Characteristic amplitude and timescales in the step response of a second order system. η_o, η_{ss} are the overshoot and steady state values, respectively, and t_r, t_p, t_s are the rising, peak, and settling times, respectively. The steady state height is $\eta_{ss} > h$ as the piston wavemaker moves constantly at U_G .

shown in Fig. 3(a), and given by

$$U_G(t) = U_0\Theta(t), \quad (10)$$

where $\Theta(t)$ is the Heaviside function. The step value is 0 for negative times and $U_G = U_0$ for positive times, resulting in a linear displacement $X_G(t)$ of the piston wavemaker. In this part of the study, we set the tank length to $L = 4$ m, the tank height to 0.25 m, and the mean still water level to $h = 0.15$ m. Mesh M_U^1 is the coarsest and M_U^6 the finest. M_{NU}^7 to M_{NU}^9 are non-uniform meshes as previously described. They use a cell size at the wall defined later on in the conclusion of the uniform mesh study and geometric growth rate $r = 1.05$ in the x-direction and $r = 1.2$ in the z-direction. For the finest mesh in the z-direction (mesh M_U^6), it is necessary to reduce the time step to keep the Courant number below 1. This is why the time step is set for all meshes to $\Delta t = 10^{-4}$ s. The measured quantity is the water elevation at the wavemaker η_w . The variables of interest are described in Fig. 3(b) and are the following: η_o, η_{ss} , the overshoot and steady state values, respectively, and t_r, t_p, t_s , the rising, peak, and settling times, respectively. Results are reported in Table I and shown in Fig. 4. Figure 4(a) shows the time series of the water elevation at the piston wavemaker, $\eta_w(t)$, for each mesh. The results of the four finest meshes are similar. A Grid Convergence Index (GCI) study³⁶ is carried out with meshes 4, 5, and 6. The local order of accuracy p ranges from 0.18 to 17.57 with a global average of 4.98. This apparent average order is used to assess the GCI error at every point as suggested in Ref. 36. The error made in the last mesh is really low (the maximum GCI error is 0.3%), which allows us to say that the results do not depend on the mesh. Figure 4(b) shows the error for every point, and a zoom around the overshoot is displayed in the inset where errors increase. The mean error is an order of magnitude lower (0.03%). The errors on the overshoot and the steady state values are very low. Figures 4(c) and 4(d) show the convergence of the different parameters composing the typical response

to the step (overshoot and steady state water elevation, rising, peak, and settling times). They show that for these parameters, the limit of convergence is mesh M_U^3 . It is chosen, for obvious practical reasons, to work with mesh M_U^3 at the wavemaker, which allows us to decrease computational times while assuring convergence. Non-uniform mesh shows good agreement with the uniform ones for all variables. In the rest of this work, we make sure that the first cell at the piston wavemaker wall is kept below $\Delta x_w = 0.0025$ m in the x-direction and $\Delta z = 0.001$ m in the z-direction in order to keep the results independent of the mesh. The number of cells per wavelength and height in the wave propagation zone is analyzed in the following paragraph.

2. Wave propagation

In order to properly study the wave propagation properties as a function of the mesh type and quality, we use an extended wave tank with $L = 8$ m. The mesh is finer at the water–air interface and is kept uniform in the zone where the wave propagates. At the wavemaker, we set $\Delta x_w = 0.001$ m, and a transition is made with a 1.05 cell to cell ratio. The piston stroke is set to $X_0 = 0.004$ m, the wavemaker frequency to $f = 1.25$ Hz, and the piston wavemaker velocity to $U_G(t) = X_0\omega/2 \sin(\omega t + \delta)$ with $\delta = -\pi/2$. The corresponding wavelength can be estimated from the dispersion relation $\omega^2 = gk \tanh(kh)$, where k is the wave number, and in this case, $\lambda = 0.82$ m. A common discretization is given by 20–25 elements per wave height and 60–70 elements per wavelength in recent works.³⁷ We conduct our test based on three meshes whose properties are shown in Table II, where M_{NU}^7 is the coarsest mesh and M_{NU}^9 the finest one. The number of cells per wave height ranges from 15 to 60, while the number of cells per wavelength ranges from 60 to 240. The time step is set to $\Delta t = 0.001$ s, and the theoretical CFL number is reported. Even if it shows to have a value below 1, the time step for the finest mesh M_{NU}^9 had to be decreased

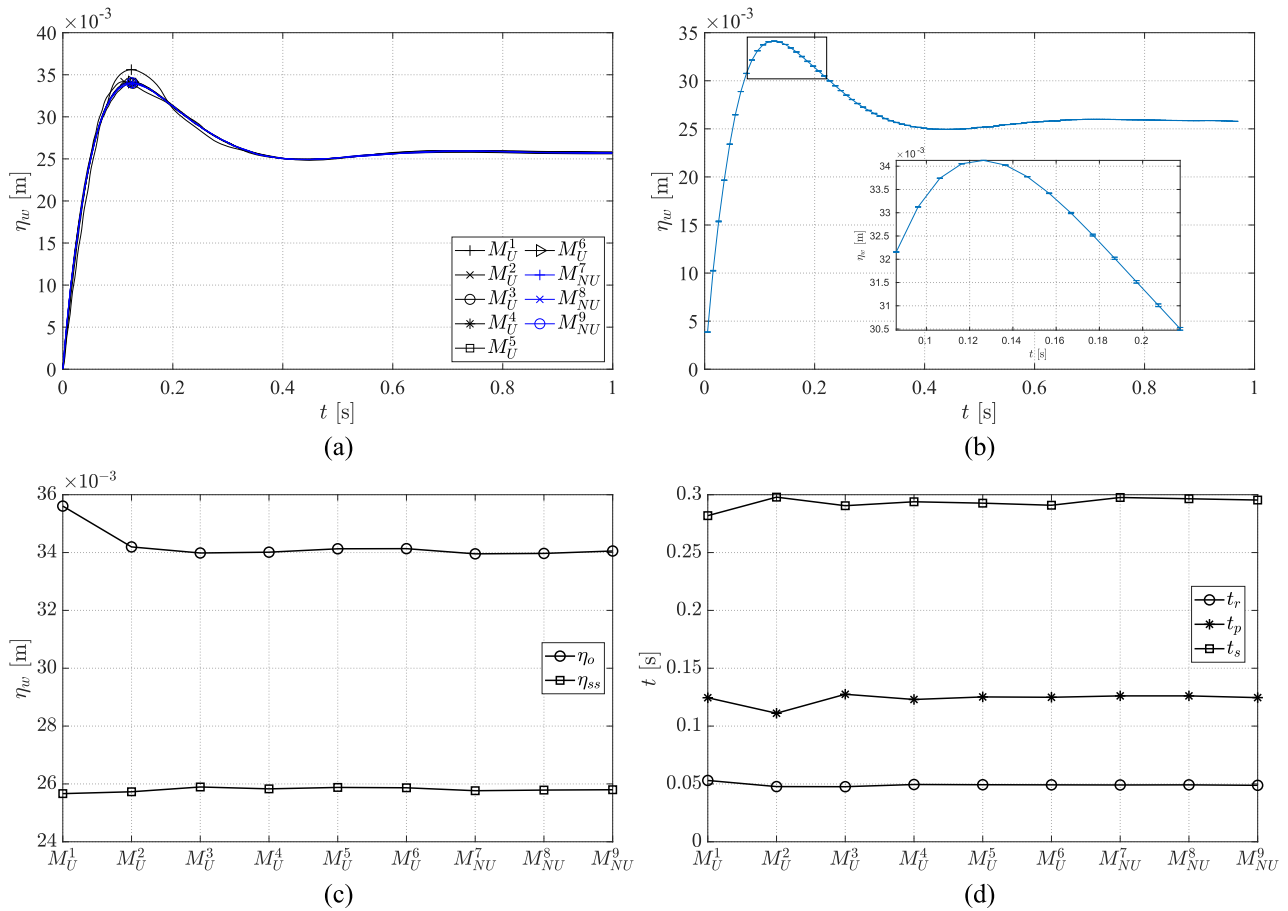


FIG. 4. Step response. (a) Water height at the piston wavemaker for different meshes. Convergence is achieved from mesh M_U^3 . (b) Error made due to mesh discretization calculated with the GCI method.³⁶ A zoom in the overshoot region is also displayed. (c) Overshoot and steady state water height (η_o and η_{ss} , respectively) as a function of the mesh. These variables seem to have converged at mesh M_U^3 . (d) Characteristic times (rising time t_r , peak time t_p , and settling time t_s) as a function of the mesh type. Converged values are found from mesh M_U^3 .

to $\Delta t = 0.0005$ s to avoid divergence due to the use of explicit schemes. The simulation end time is 10 s, and two probes are set at $x = 2$ m and $x = 4$ m from the origin of the coordinate system (cf. Fig. 1).

TABLE II. Mesh characteristics and their theoretical CFL number for the wave propagation problem.

	M_{NU}^7	M_{NU}^8	M_{NU}^9
Cells/ H	15	30	60
Cells/ λ	60	120	240
Δx_w (m)	0.001 00	0.001 00	0.001 00
Δx (m)	0.013 60	0.006 80	0.003 40
Δz (m)	0.000 30	0.000 15	0.000 07
Total number of cells	40 734	107 184	303 232
CFL number	0.15	0.29	0.59

Figure 5(a) shows the water level at the wavemaker wall $\eta_w(t)$. No differences between the meshes are observed as expected, since the refinement in the x -direction and in the z -direction is finer than the necessary one studied in (i). Figure 5(b) shows the differences between the meshes that are used at $x = 4$ m. A zoom over the highest value and for three wave periods is shown in Fig. 5(c). The coarse mesh M_{NU}^7 effectively produces minor differences from the other two, specially at the maxima and minima. The results for the probe at $x = 2$ m are compared with the theory in Ref. 6 and shown in Fig. 5(d). The errors of wave crests and troughs with the wavemaker theory are shown in Table III. The results are quite accurate for the three meshes (almost all cases with a rms deviation below 0.1 mm) although the coarse mesh lacks accuracy at the maxima and minima. It is chosen to work with the medium mesh M_{NU}^8 in the rest of this work as it allows accurate wave height data and reduces the computational time compared to the fine mesh. The final mesh characteristics are given in Table IV.

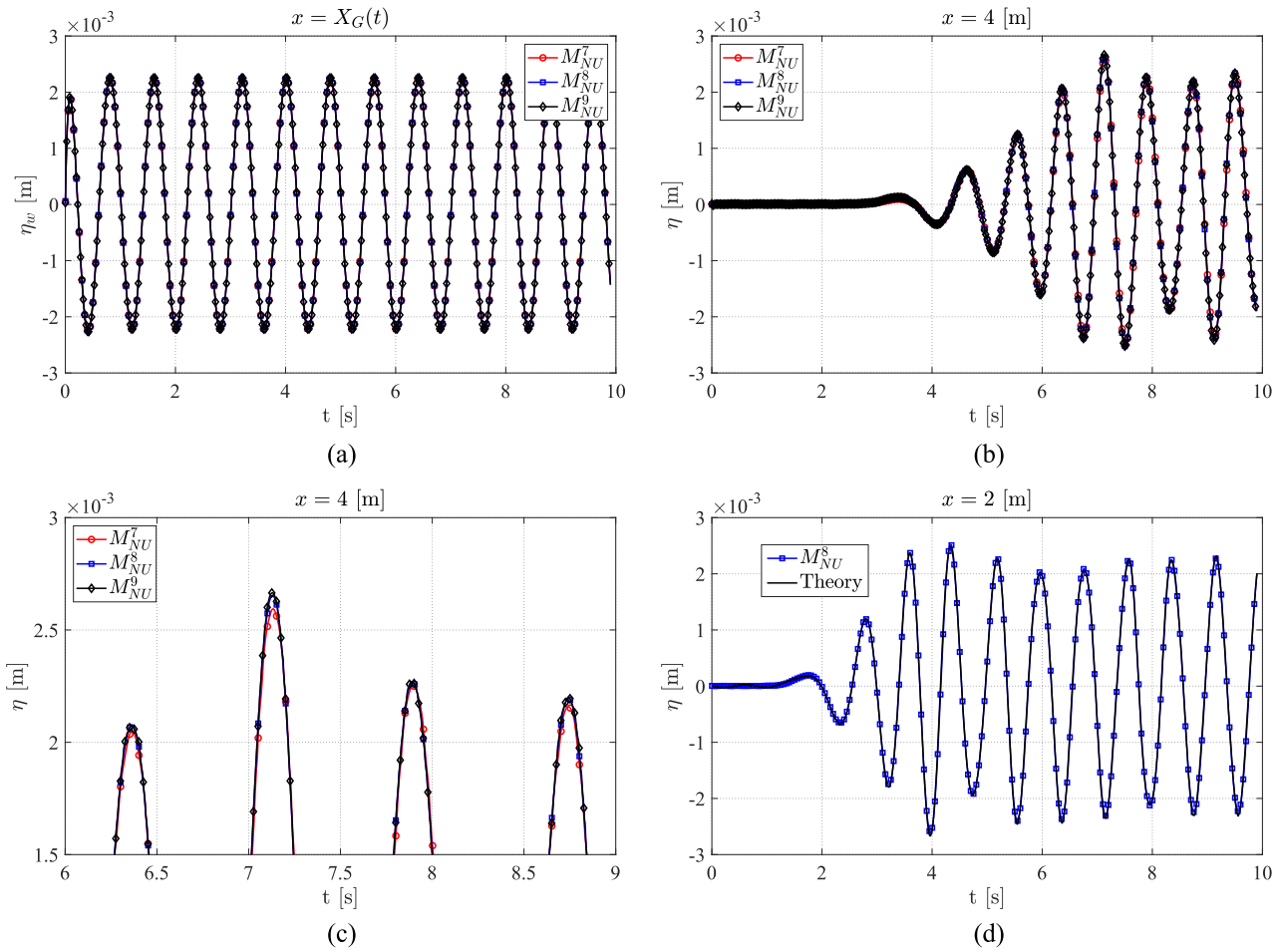


FIG. 5. Continuous wave propagation. (a) Water height at the piston wavemaker η_w as a function of time. (b) Water height at $x = 4$ m as a function of time. (c) Water height at $x = 4$ m as a function of time, with a zoom over times between 6 s and 9 s. (d) Comparison between the medium mesh and the wavemaker theory⁶ at $x = 2$ m. The medium mesh well represents the wavemaker theory. It allows us to validate the wave generation process with the medium mesh for small waves.

TABLE III. rms deviation relative to the theory in Ref. 6 over the 10 s simulation for both wave gauges at $x = 2$ m and $x = 4$ m. The rms deviation is calculated according to $\Delta_{RMS} = \sqrt{\sum_{j=1}^N (\eta_j - \eta_j^{theo})^2} / N$.

	$\Delta_{RMS}(x = 2m)$ (m)	$\Delta_{RMS}(x = 4m)$ (m)
M_{NU}^7	7.2×10^{-5}	1.10×10^{-4}
M_{NU}^8	4.3×10^{-5}	0.80×10^{-4}
M_{NU}^9	4.4×10^{-5}	0.83×10^{-4}

TABLE IV. Characteristics of the final mesh.

Δx_w (m)	Cells/ λ	Cells/ H	r_x	r_z
0.001	120	30	1.05	1.20

III. RESULTS

One of the objectives in this work is to characterize the piston wavemaker system by applying a series of velocity steps. First, a qualitative approach is taken and observations are made about the wave generation at small times and the generated wave pulse is studied at longer times and far away from the wavemaker. Then, we compare the characteristic variables with the theory developed in Ref. 11 and explore higher Froude number regimes. The forces exerted on the wavemaker and the power involved in the wave generation process are studied, and an active wave absorption strategy is finally designed. The step velocity tests are carried out at four mean still water levels: $h = 0.050$ m, 0.075 m, 0.100 m, 0.150 m, and for velocities ranging from $U_G = 0.005$ m/s to $U_G = 0.4$ m/s. In this problem, the fundamental velocity, length, and timescales are \sqrt{gh} , h , and $\sqrt{h/g}$, respectively. The problem can be written as $f(\eta_w, \rho, g, h, t, U_G) = 0$, but according to the Buckingham π theorem,³⁸ it can be reduced to $f(\eta_w^*, t^*, Fr) = 0$, where η_w^* and

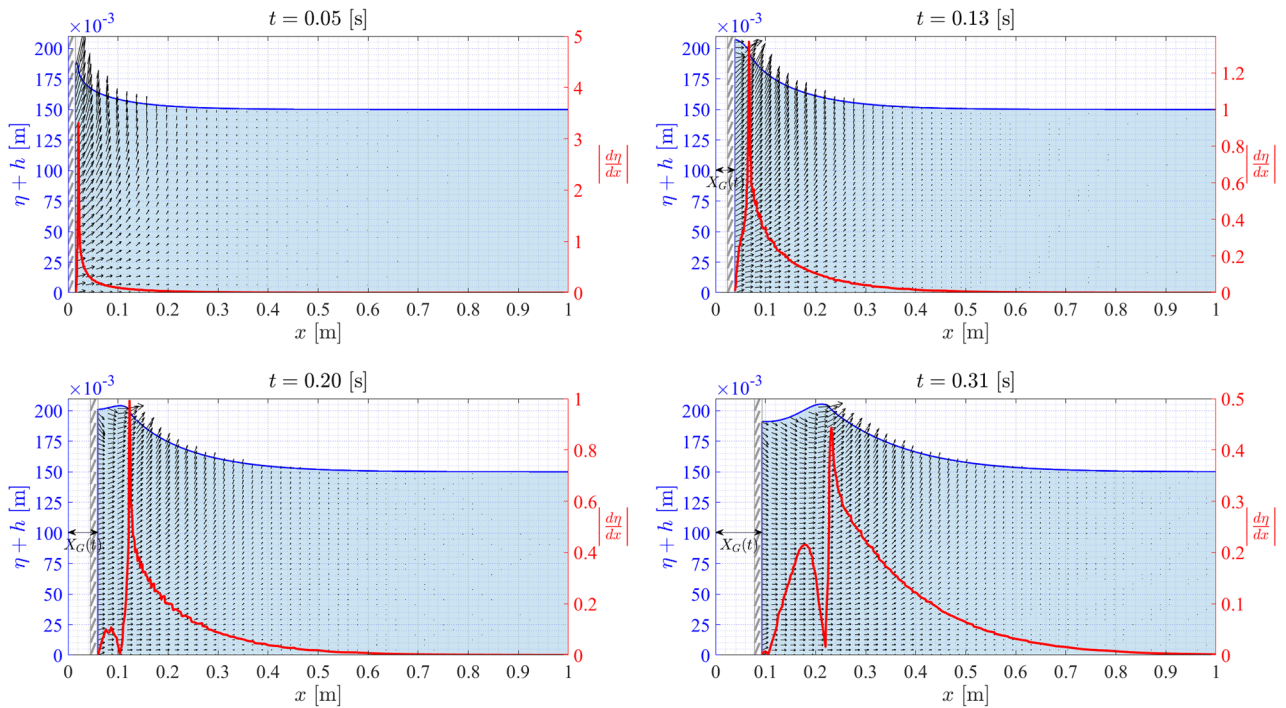


FIG. 6. Time snapshots of the wave pulse generated (from left to right) by a velocity step applied to the wavemaker motion. The wave pulse is called here the overshoot-wave as it is created by the overshoot of the water elevation at the piston wall. The wave profile (wave height as a function of x) is plotted in blue and the wave steepness as a function of x in red. The velocity step is 0.3 m/s, and the mean still water level h is 0.15 m. The shown times are $t = 0.05 \text{ s} \approx t_r$, $t = 0.13 \text{ s} \approx t_p$, $t = 0.20 \text{ s}$, and $t = 0.31 \text{ s} \approx t_s$.

t^* are the dimensionless water height at the piston wavemaker and time, respectively. In the next sections, as a consequence of this analysis, we will express the results in a dimensionless way using the relevant variables η_w^* , t^* , and Fr .

A. First instants—The overshoot-wave

While applying a velocity step to the wavemaker, one observes the formation of a surface water pulse propagating along the tank as it is shown in Figs. 6 and 7. The wavemaker displaces a given

volume of water, and as the fluid is incompressible, this volume is found under the wave profile. The water height at the wavemaker $\eta_w(t)$ first rises along the wall reaching a maximum value, the overshoot. Then, the wave pulse comes off the wall and self-propagates in the positive x -direction, as the phase velocity of the wave becomes higher than the wavemaker velocity $C_p > U_G$. In the time snapshots in Fig. 6, the wave pulse generated by the velocity step is called the overshoot-wave as it is created by the overshoot of the water elevation at the piston wall.

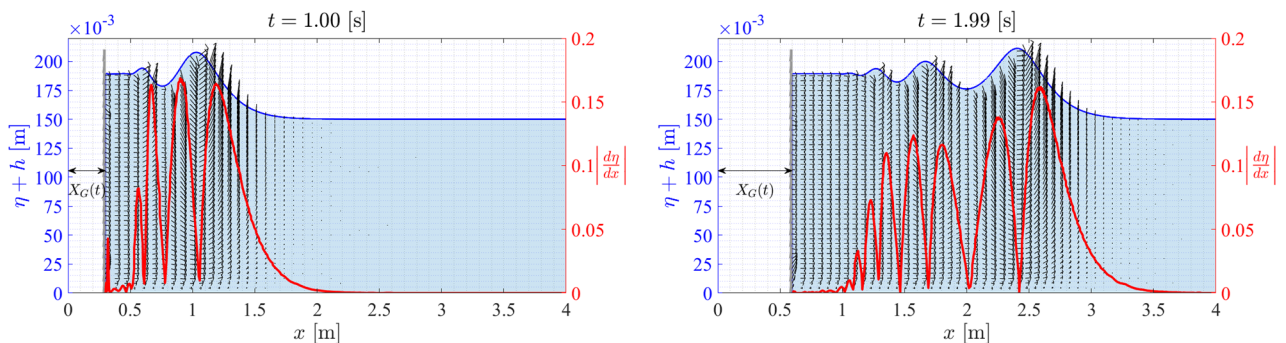


FIG. 7. Snapshots at times $t = 1.00 \text{ s}$ and $t = 1.99 \text{ s}$ of the wave pulse generated (from left to right) by a velocity step applied to the wavemaker motion. The wave profile (wave height as a function of x) is plotted in blue and the wave steepness as a function of x in red. The velocity step is 0.3 m/s, and the mean still water level h is 0.15 m. Note the change in scale in the x abscissa compared to Fig. 6.

After leaving the wavemaker, the water height at the wavemaker remains constant, as indicated in Fig. 9. The wave pulse profile for times $t = 0.05$ s, 0.13 s, 0.20 s, 0.31 s, which correspond to the first instants of the pulse formation, is displayed in Fig. 6. In Fig. 6, the wave steepness, defined as $|d\eta/dx|$, is superimposed. We observe that the wave steepest shape occurs at the very first instants of its formation, i.e., at $t = 0.05$ s, where the maximum steepness is higher than 3. When the pulse starts leaving the piston wavemaker, its steepness decreases to values under 1. Such high steepness is associated with the non-linear properties of the overshoot-wave. Another important parameter useful to evaluate when it comes to apply linear theory is the wave height to mean still water level ratio η/h . It is relatively important (values around 0.5 in this example); therefore, Airy theory of linear waves cannot be applied here. The profile of the generated pulse at longer times is shown in Fig. 7, as well as its steepness as a function of the x -coordinate. We can notice the generation of wiggles after the main pulse propagating downstream as already described. The wiggles are trailing waves whose height decreases in the vicinity of the piston wavemaker, while the front wave height increases as it travels. These wave structures are described in the work of Ref. 11 and are a consequence of wave dispersion. The piston motion creates a wave packet in which each wave travels at different velocities due to dispersion effects. We identify the created wave to be an undular bore, which was experimentally and theoretically studied in Refs. 39 and 40, respectively, while Stoker⁴¹ predicted that an impulsive wavemaker would generate an undular bore as in the present case. Recently, similar bore structures were obtained from a different approach where a moving weir at the bottom of a channel may produce the volumetric water displacements necessary to develop such a wave.⁴²

Undular bores are of particular importance as they appear to more likely represent a real tsunami wave instead of a solitary wave.⁴³ Important values of the wave steepness are observed during the pulse formation, which decrease rapidly as the pulse propagates without evidence of wave breaking. If the bore strength is important, undular bores may display a wave breaking process.⁴² In the time snapshots in Figs. 6 and 7, we observe the vector velocity field of the numerical solution of the Navier–Stokes equations. The vector field becomes intense precisely near the steepness peaks as the overshoot-wave propagates along the tank. The higher the wave height, the higher the intensity of the vector field, which is associated with particle velocity.

The starting overshoot-wave displays a phase celerity C_p as a function of time t , which may be compared with two characteristic properties, the shallow water wave speed $C_p = \sqrt{g(h+H)}$ and the piston velocity U_G , as shown in Fig. 8. The overshoot-wave celerity may be estimated from the mean celerity as $C_p = \delta x / \delta t$ between consecutive wave crests or looking for maximum steepness at different time steps during the propagation, as shown in Fig. 6. As the phase celerity of the overshoot-wave is found to be higher than the piston velocity from the first instants of motion, the overshoot-wave travels fast enough to leave the piston wavemaker. As the wave propagates along the tank, its phase celerity increases with time, approaching the shallow water phase speed given by $C_p \rightarrow \sqrt{g(h+H)}$. This behavior agrees with that in potential theory and therefore allows us to validate the capabilities of the numerical wave tank for wave propagation.

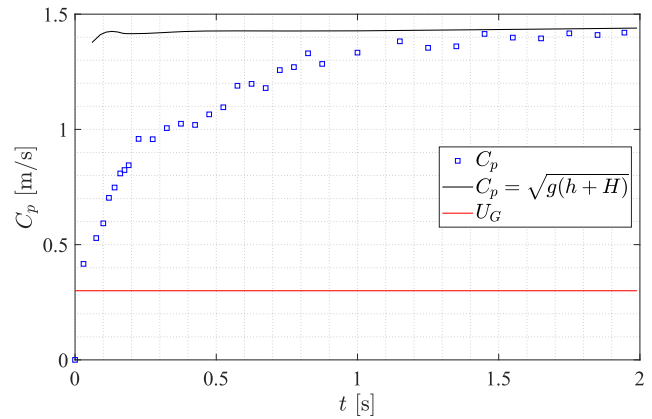


FIG. 8. Instantaneous overshoot-wave phase celerity $C_p(t)$ (in blue) as a function of time for the case $h = 0.15$ m and $U_G = 0.3$ m/s. For times lower than 0.2 s, the maximum of the steepness is used to determine the location of the overshoot-wave. For later times, the maximum of the wave profile is taken as the location of the wave. The wave celerity can be compared to the piston step velocity U_G and to the phase velocity of shallow water waves.

B. Response to a velocity step

A positive velocity step ($U_G > 0$) creates a water pulse, which leaves the wavemaker wall as it propagates along the tank. The step response is recorded as the water height or water elevation at the wavemaker wall $\eta_w(t)$ and is presented in Fig. 9(a).

The water height first increases, reaching a maximum or overshoot η_o at peak time t_p , before approaching a lower steady state value η_{ss} . It is of particular interest to note the similarity of this dynamic response to a step response of the second order system [cf. Figs. 9(a) and 3(b)]. The time response of second order linear systems depends on the type of the input signal. For a step input, the system exhibits a characteristic response defined by the rising time t_r , the maximum overshoot η_o , and the steady state value η_{ss} obtained at a given settling time t_s .²⁸ In Fig. 9(b), we present the normalized time response using the Froude number as in the theory proposed in Ref. 11. We can observe that after reaching its maximum value, the overshoot, the water height slightly oscillates and decreases to its steady state value $\eta_{ss} = hFr$. The step response for small Froude numbers found in this work is in agreement with that in the theoretical work of Ref. 11. Nevertheless, some differences with the theory are observed in the overshoot behavior for higher Froude numbers. The overshoot starts to increase beyond the theoretical prediction, and the steady state value approaches a slightly higher value than the expected one from theory, $\eta_{ss} = hFr$, as we will discuss in Sec. III B.

The relative deviation from theory¹¹ is presented in Table V for the four mean still water levels and the velocity range from 0.005 m/s to 0.3 m/s. The relative deviations are defined as $\Delta_o = |\eta_o - \eta_o^{ref}| / \eta_o^{ref}$ and $\Delta_{ss} = |\eta_{ss} - \eta_{ss}^{ref}| / \eta_{ss}^{ref}$, where the superscript *ref* refers to the study of Ref. 11. The arrows indicate how the Froude number changes while varying the step velocity or the mean still water level. It is interesting to note that the relative deviation stays low for the steady state value (< 10.5% for all velocities and mean still water levels). For both overshoot and steady state values, the

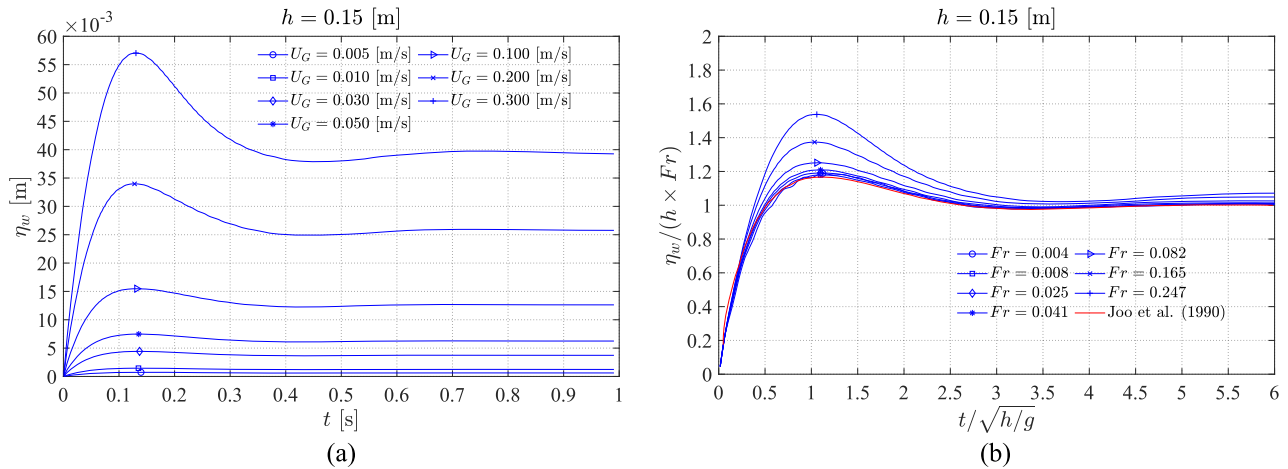


FIG. 9. (a) Water height at the wavemaker as a function of time. (b) Non-dimensional water height as a function of non-dimensional time. A comparison between the CFD simulation and the theoretical study carried out in Ref. 11 is shown.

deviation decreases with the increase in the water level (which actually corresponds, for a given step velocity, to lower Froude numbers). Finally, the deviation for the overshoot value can reach high values (> 40%) for the highest Froude numbers (high velocity, low mean still water level).

The dominant controlling parameter in this work is the Froude number Fr defined as the ratio between inertial ($\rho h^2 U_G^2$) and gravitational ($\rho g h^3$) forces, and thus, $Fr = U_G / \sqrt{gh}$. The similarity of the system response to the typical second order response under a step velocity can be analyzed through the characteristic timescales and maximum overshoot of the response. Timescales as well as the amplitude of the water height response must be plotted as a function of the step velocity U_G . As in many feedback control systems, the time response of a second order system will be completely determined when one knows the maximum overshoot η_o , the steady state amplitude η_{ss} , and the rising, peak, and settling times t_r, t_p, t_s , respectively. If the time response

is correctly described by the second order response, we should find a scaling law for the characteristic timescales at different water depths h and step velocities U_G otherwise said the Froude number.

The overshoot η_o as a function of the step velocity U_G is plotted in Fig. 10(a) and the steady state η_{ss} is plotted in Fig. 10(c), both for two mean still water levels $h = 0.05$ m and $h = 0.15$ m. The steady state values evolve linearly with the generation step piston velocity as they correspond to the water height of the displaced volume, which increases linearly in time as the step velocity U_G is constant for $t > 0$. However, the overshoot dependence on U_G is not linear as the overshoot-wave originates during a rapid transient process. The curve collapse under the proposed scaling is relatively good in the range of mean still water levels shown as $0.05 \leq h \leq 0.15$ m. The scaling for the overshoot fails when $Fr > 0.2$ as the overshoot-wave height increases over the linear limit and starts to move faster with higher U_G .

TABLE V. Relative deviation from the model of Ref. 11 at different water depths and step velocities ($0.005 < U_G < 0.3$ m/s). The relative deviation is defined as $\Delta_o = |\eta_o - \eta_o^{ref}| / \eta_o^{ref}$, $\Delta_{ss} = |\eta_{ss} - \eta_{ss}^{ref}| / \eta_{ss}^{ref}$. The superscript *ref* refers to the study of Ref. 11. The arrows indicate how the Froude number varies with the step velocity and the mean still water level.

U_G (m/s)	$h = 0.05$ (m)		$h = 0.075$ (m)		$h = 0.10$ (m)		$h = 0.15$ (m)		
	Δ_o (%)	Δ_{ss} (%)	Δ_o (%)	Δ_{ss} (%)	Δ_o (%)	Δ_{ss} (%)	Δ_o (%)	Δ_{ss} (%)	
Fr ↓	0.005	5.97	1.86	2.42	0.09	3.64	3.96	1.77	0.61
	0.010	3.33	1.19	2.14	0.16	1.15	0.34	0.98	0.39
	0.030	3.69	1.35	3.26	0.80	2.79	0.85	2.00	0.82
	0.050	5.98	2.40	5.09	1.48	4.54	1.60	3.54	1.26
	0.100	11.96	4.11	10.60	3.42	9.33	2.81	7.20	2.37
	0.200	25.73	7.00	23.02	5.97	20.77	5.35	17.64	4.52
	0.300	43.67	10.48	40.42	8.75	37.72	7.72	31.67	6.39
← Fr									

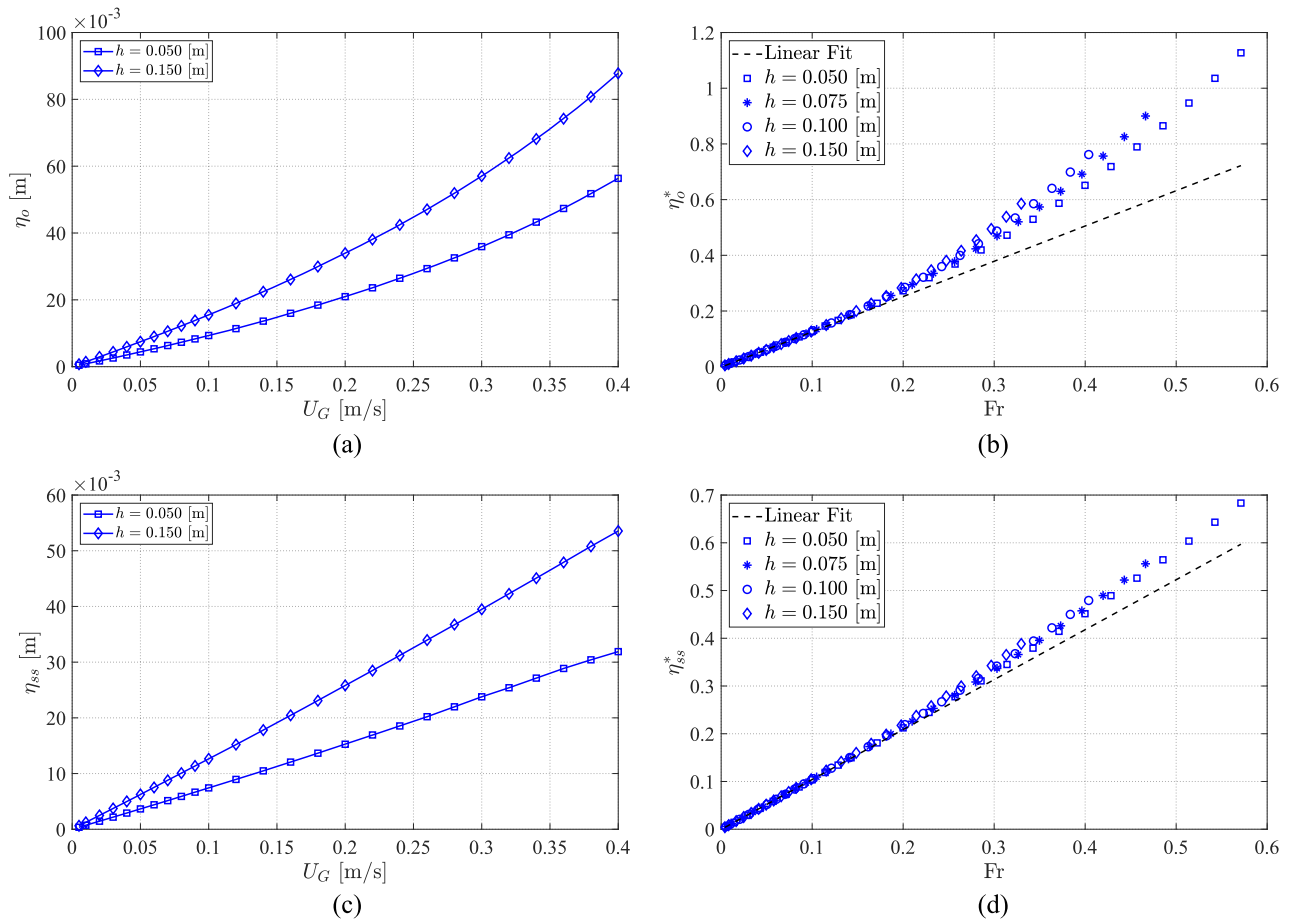


FIG. 10. (a) Overshoot η_o of the water elevation at the piston wall as a function of the piston step velocity U_G . Two still water levels are considered: 0.05 m and 0.15 m. (b) Dimensionless overshoot at the piston wall $\eta_o^* = \eta_o/h$ vs Froude number. A linear fit for low Froude number $Fr < 0.1$ is drawn as a dashed black line for comparison and is given by $\eta_o^* = 1.267 \cdot Fr - 0.0015$ and $R^2 = 0.9994$. (c) Steady state water elevation η_{ss} as a function of the piston step velocity U_G . Two still water levels are considered: 0.05 m and 0.15 m. (d) Dimensionless water height steady state at the piston wall $\eta_{ss}^* = \eta_{ss}/h$ vs Froude number. A linear fit for low Froude number $Fr < 0.1$ is drawn as a dashed black line for comparison and is given by $\eta_{ss}^* = 1.046 \cdot Fr - 0.0005$ and $R^2 = 0.9997$. The different still water levels are represented with symbols.

The evolution of the characteristic timescales of the response to a velocity step is shown in Fig. 11. As it is indicated in Fig. 3, these timescales are associated with a second order dynamical response, where the water height at the piston wall η_w is measured and compared to the steady state height η_{ss} . The rise time t_r and the peak time t_p are associated with the very first instants of the wave motion, when the overshoot-wave is created. Both time constants appear to be independent of the step velocity and provide an interesting scaling independent of the Froude number where the dimensionless timescale is written as

$$t^* = \frac{t}{\sqrt{h/g}}. \tag{11}$$

As shown in Fig. 9, after the main wave leaves the piston zone, the water height on the piston wall scales perfectly with the Froude number as $\eta_w/(hFr) = 1$ because the displaced volume in the steady

state regime is entirely determined by the steady state water elevation η_{ss} . The associated settling time t_s is computed within a 10% band and slightly grows with the Froude number. In Fig. 11(b), the time scaling indicated in Eq. (11) produces a very tight collapse of each characteristic time as a function of the Froude number.

The scaling seems to confirm the similarity of the water elevation response with a second order response. As the wave pulse is created by the excess or overshoot of the water elevation at the piston wall, we called it the overshoot-wave. The piston motion produces the displacement of a water volume (per unit depth) given by $V(t) = U_G t h$, which displays an initial transient peak, the overshoot, superimposed into a water slug rising over the mean still water level h . The overshoot-wave has its own dynamics, moving at shallow water speed, running over the water slug, and therefore leaving the displaced volume faster than the linear waves.

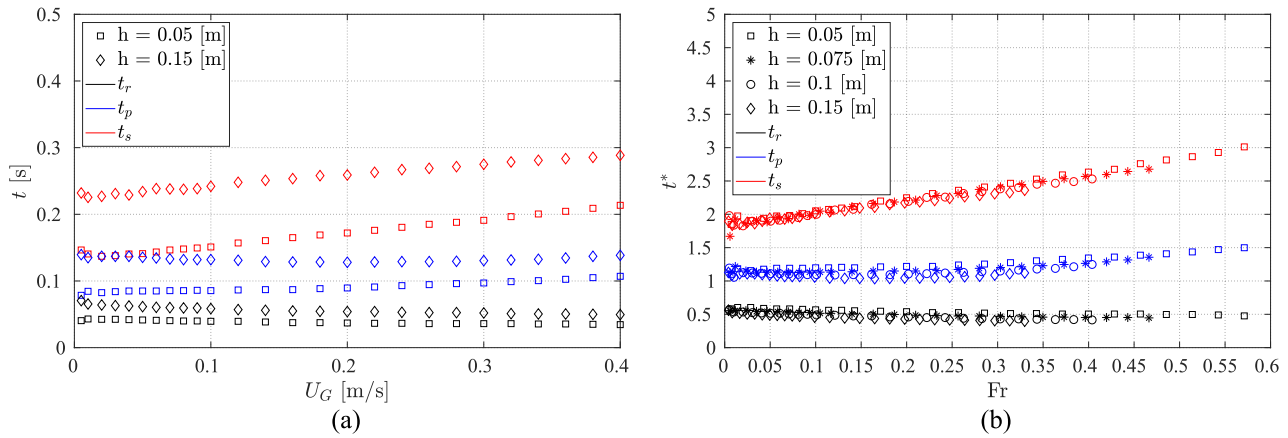


FIG. 11. (a) Characteristic timescales as a function of the wavemaker step velocity U_G . (b) Dimensionless characteristic timescales $t^* = \frac{t}{\sqrt{h/g}}$ as a function of the Froude number.

C. Forces involved in the step response

In this section, we present new findings such as the force decomposition and the maximum power as a function of the Froude number. The objective of this section is to determine the forces originated on the piston wavemaker during the step response. As the problem is 2D, there are only two components of the forces projected on the piston wall in the x-direction and z-direction, which are inertial, pressure, and viscous forces. These forces can be calculated from the pressure and velocity fields at the wavemaker using the stress tensor $\underline{\underline{\varepsilon}}$, the elementary surface area dS (which is in the 2D case an elementary length), and its normal \mathbf{n} ,

$$\mathbf{F}_w = \int_z \underline{\underline{\varepsilon}} \cdot \mathbf{n} dS. \tag{12}$$

The stress tensor is defined as

$$\underline{\underline{\varepsilon}} = -p \begin{bmatrix} 1 & 0 \\ 0 & 1 \end{bmatrix} + 2\mu \begin{bmatrix} \frac{\partial u_x}{\partial x} & \frac{1}{2} \left(\frac{\partial u_z}{\partial x} + \frac{\partial u_x}{\partial z} \right) \\ \frac{1}{2} \left(\frac{\partial u_z}{\partial x} + \frac{\partial u_x}{\partial z} \right) & \frac{\partial u_z}{\partial z} \end{bmatrix}. \tag{13}$$

In Fig. 12, we display the resulting normal and tangential force profiles [$f_x(z)$ and $f_z(z)$, respectively] as a function of the vertical coordinate starting from the bottom of the tank and across both fluid phases. As the mean still water level is $h = 0.15$ m, we note a marked change at the air–water interface $z = 0.15$ m on both types of forces. However, as expected, there is approximately a five orders of magnitude difference between both components. The normal force profile $f_x(z)$ is mainly hydrostatic and insensitive to time, and the viscous or tangential force profile $f_z(z)$ is dependent on time at low U_G values. Wall shear is created during the formation of the overshoot-wave, which indicates the positive increase in the resulting vertical

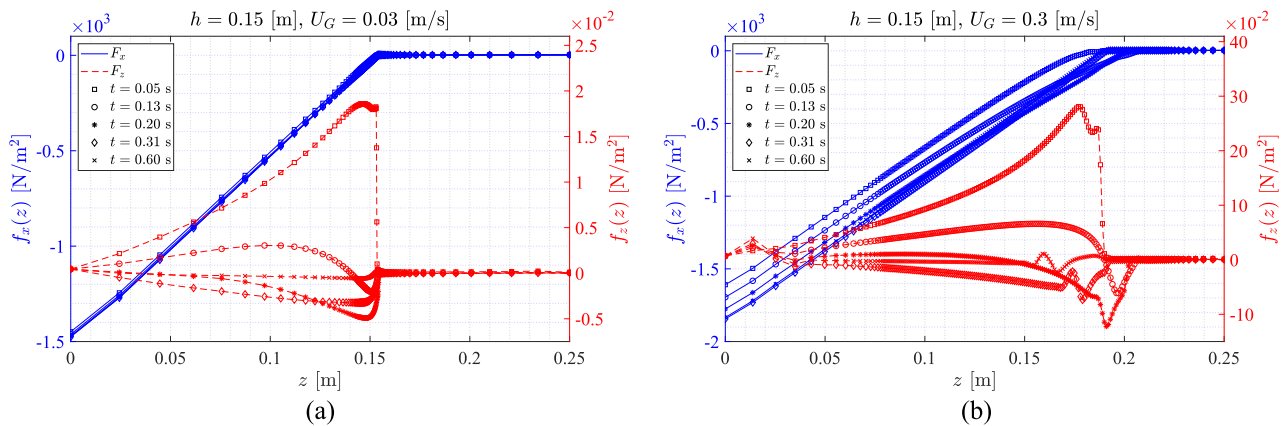


FIG. 12. Normal and tangential force profiles (along the z axis, f_x and f_z , respectively) per unit area at the wavemaker for times 0.05 s, 0.13 s, 0.20 s, 0.31 s, and 0.60 s and $h = 0.15$ m. Notice the difference of power of ten between the two plot vertical axes. (a) $U_G = 0.03$ m/s. (b) $U_G = 0.30$ m/s.

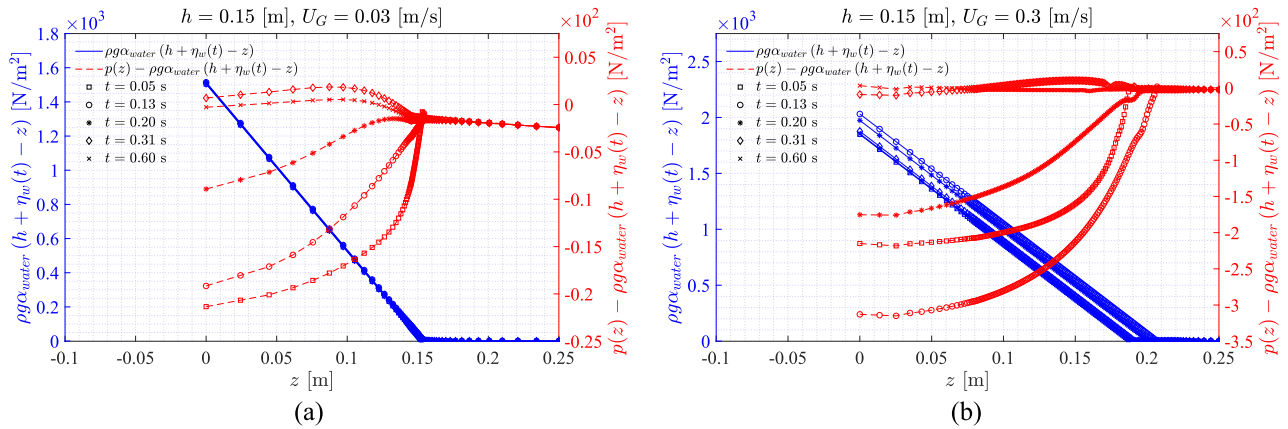


FIG. 13. Pressure forces [hydrostatic $\rho g(h + \eta)$ and $p - \rho g(h + \eta)$] (along the z axis) at the wavemaker for times 0.05 s, 0.13 s, 0.20 s, 0.31 s, and 0.60 s and $h = 0.15$ m. (a) $U_G = 0.03$ m/s. (b) $U_G = 0.30$ m/s.

force $F_z(z)$ in Fig. 14(b). When the overshoot-wave leaves the piston, and the progressing volume pushed by the piston reaches a steady state motion, the shear forces become very small. When the step velocity is increased to $U_G = 0.3$ m/s, the normal force profile $f_x(z)$ displays notorious changes in time but finally evolves into an almost hydrostatic vertical profile, as shown in Fig. 13(b).

In order to verify the effects of the initial fluid motion on the pressure field during the step response, we recorded the pressure profiles at both step velocities $U_G = 0.03$ m/s and $U_G = 0.3$ m/s. The sudden increase in water elevation at the piston wall is more important at higher U_G , which is explained by the higher volume displaced during the initial times. Shear forces change in sign during the formation of the overshoot-wave, as shown in Fig. 12 at both step velocity values. The first water elevation motion produces a positive shear on the piston wall and therefore a positive shear force, which start to decrease, becoming negative as the overshoot-wave

leaves the piston wall and the force points downward before vanishing in the steady state regime. The pressure profile is dominated by hydrostatics, as shown in Fig. 12. However, when we subtract hydrostatic pressure due to the initial wave elevation along the z axis, i.e., we plot $p(z) - \rho g(h + \eta)$, we observe traces of the creation of the overshoot-wave on the remanent pressure. As time progresses and the overshoot-wave leaves the piston wavemaker, this remanent dynamic pressure contribution approaches very low values with respect to hydrostatics.

In order to compute the power delivery involved in the process, we must get a good estimate of the resulting forces on the piston. In Fig. 14, we present the normal and tangential forces on the piston wall as a function of time, uncovering the initial transient associated with the overshoot-wave formation and during the steady state regime. The normal and tangential force profiles are obtained integrating the force profiles in Fig. 12 along the piston

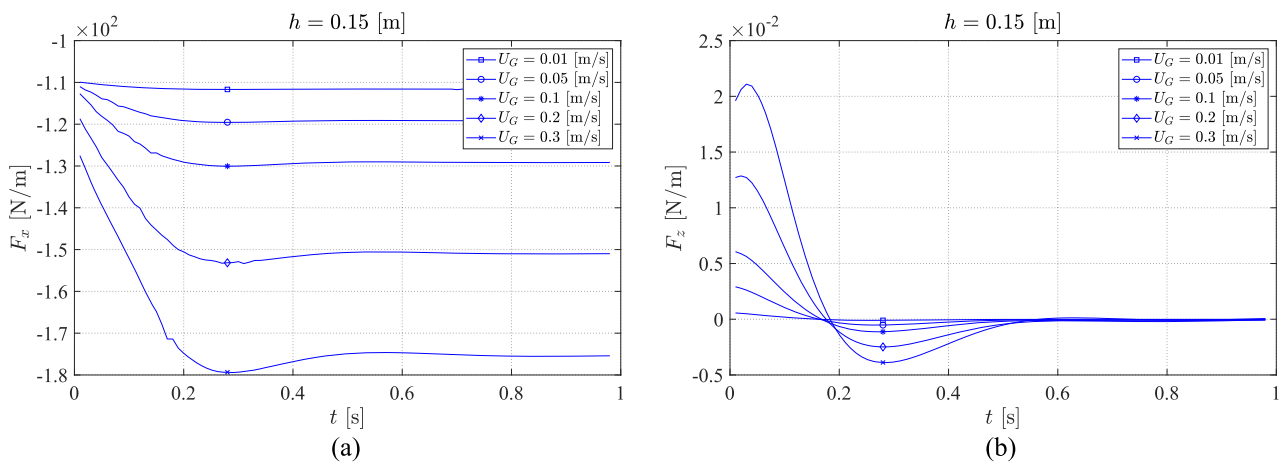


FIG. 14. Resulting net forces per unit length as a function of time. (a) Normal net force $F_x(t)$ and (b) tangential net force $F_z(t)$. The mean still water level is $h = 0.15$ m, and the step velocity range is $0.01 \text{ m/s} \leq U_G \leq 0.3 \text{ m/s}$.

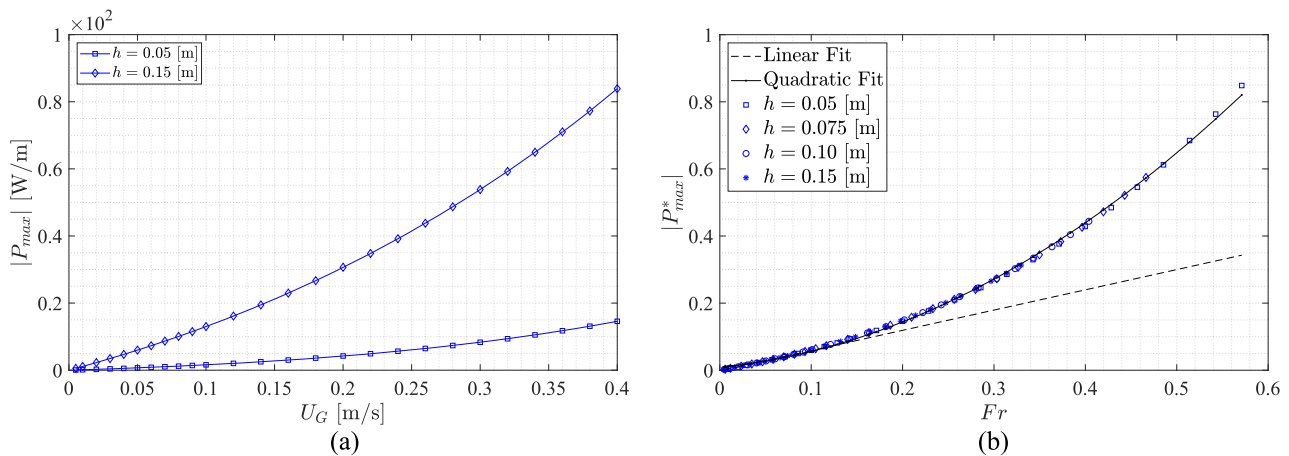


FIG. 15. Power delivery during wave generation. (a) Maximum power per unit length P_{max} vs step velocity U_G at $h = 0.05$ m and $h = 0.15$ m. (b) Dimensionless maximum power per unit length P_{max}^* as a function of the Froude number Fr at different mean still water levels. A quadratic fit is carried out and gives $P^* = 2.0079Fr^2 + 0.2740Fr + 0.0087$ (with the correlation coefficient $R^2 = 0.999\ 06$).

wall during each time step, providing an accurate estimation of the net forces shown in Fig. 14. The resulting normal forces $F_x(t)$ are negative as they oppose the piston motion. If we plot the absolute values, we find a time evolution very similar to that of water elevation $\eta_w(t)$ in Fig. 9. The first rising part is associated with the force excess resulting from the creation of the overshoot-wave followed by a steady state force associated with the progressive motion of the mass of the water slug moving at constant velocity U_G . On the other side, the tangential averaged forces $F_z(t)$ shown in Fig. 14 display a change in sense (sign), indicating how the fluid is moving on a boundary layer created on the piston wall. At first, the fluid moves upward, then stops, and then moves downward reaching a local (downward) maximum precisely when the overshoot-wave leaves the piston. The critical time when the resultant shear force is zero $t \sim 0.2$ s does not correspond to the peak time as water is still rising at the bottom of the wavemaker, as shown in Fig. 6. X-force characteristic times (rise and peak times) are much larger than those for the kinematic observations. The minimum shear force time corresponds to the maximum force in the x-direction, showing the correlation between both phenomena. We can imagine that a feedback controlled piston wavemaker might also be designed by measuring the vertical force instead of the one in the direction of the piston motion. If the overshoot-wave is going away leading to a fluid flow downward at the interface, the global motion is more complicated, with a flow still going upward at the base of the piston.

During the design of a piston wavemaker, it is important to evaluate the power input during the step response associated with the wave generation process, as it can be particularly useful in determining the scaling. For example, the *Flowave* facility power demand can creep close to 300 kW when it creates a sea state moving the 168 paddles.⁴⁴ Dimensioning the necessary power supply is then of crucial importance. This section is devoted to the evaluation of the energy input required to create a wave pulse resulting from a piston velocity step. The power involved in the step motion of the piston wavemaker is calculated according to the following equation:

$$P(t) = \mathbf{F}_w \cdot \mathbf{U}_w. \quad (14)$$

In this case, the piston wall velocity is $\mathbf{U}_w = U_G \hat{x}$, which is the Heaviside step function. Maximum power delivery as a function of the step velocity is shown in Fig. 15(a). The maximum power corresponds to the maximum water elevation at the piston wall. An expected power increase is found when the step velocity increases, but more impressive is the radical change in the power delivery when the mean still water level is increased. If we look for a scaling of the power delivery, we may use a characteristic force per unit length and velocity to perform the normalization. The normalized maximum instantaneous power can be written as

$$P^* = \frac{P}{\rho g h \sqrt{gh}} = \frac{P}{\rho g^{3/2} h^{5/2}},$$

where P is the power per unit length. The involved force is the hydrostatic pressure force, and the velocity is the corresponding shallow wave celerity \sqrt{gh} . In Fig. 15(b), the normalized maximum power P^* vs Froude number collapse for different mean still water levels confirms that the scaling has been properly defined and it follows accurately a quadratic fit (obtained by least square fitting). This law can be used as an entry design tool to define the maximum power that is necessary to generate waves.

D. Active wave absorption

An active wall driven by a feedback controller may be useful not only to cancel wave reflections but also to attenuate wave impacts associated with extreme waves on a vertical wall and reduce their consequences.⁴⁵ We have here implemented an active wave absorption strategy using our results from the response of the wavemaker to velocity steps discussed in Sec. III B. First, consider a wave created at the wavemaker, propagating from left to right, whose shape is a leading trough, as shown in Fig. 16. To absorb this wave at the right active wall, a wave crest of nearly opposite phase has to be superimposed, which is generated by the motion of a wave-absorber, a

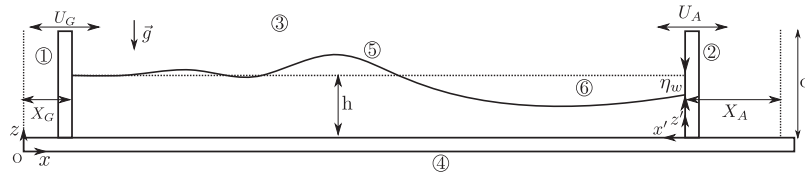


FIG. 16. Schematics of the wave absorption problem. The numerical domain is composed of (1) the piston wavemaker, (2) the piston wave-absorber on which the water level η_w is measured, (3) the atmosphere, and (4) the seabed. The generated waves (5) at the free-water surface are referenced to the mean still water level (6) h . A second frame of reference, on the wave-absorber, is indicated as (x', z') .

wavemaker situated at the right side of the tank, according to the following strategy.

Consider a wave-absorber consisting of an active flat wall with a sensor that measures the water level at the wall η_w . On the frame of reference (x', z') associated with this wave-absorber, the positive motion is from right to left (note that x' -direction is the opposite of x). The wall water level η_w can be compared to a reference value $\eta_{ref} = 0$ in order to attenuate reflections. The error $\epsilon = \eta_{ref} - \eta_w$ is permanently computed and fed into a proportional controller of gain K , which provides the absorption velocity $U_A = K\epsilon$. The corresponding block diagram of the feedback control strategy using a proportional controller is shown in Fig. 17(a). The efficiency of the control strategy relies on the choice of K where we propose to use the kinematic results of the step response rather than typical methods.²⁸ In Sec. III B, we have shown that the wall water level at the wavemaker reaches an overshoot value after a short time (as seen in Fig. 9) corresponding to the standard peak time of the system (see Fig. 11). The overshoot η_0 , the maximum water level at the wavemaker during the step, was related to the piston velocity U_G by a linear relationship at the lower part ($Fr < 0.2$) of Fig. 10(b). If we want to absorb a wave of given amplitude at the wave-absorber wall, then we are more efficient if the change in amplitude, $\eta_w \rightarrow \eta_0(U_G)$, takes into account the corresponding step velocity U_G .

The slope of the linear scaling in Fig. 10(b) (the lower part of the plot) will determine the proportional controller gain K . The absorption velocity is then computed as $U_A = K\epsilon = -K\eta_w$, where $K = 1/1.267\sqrt{g/h}$ represents the inverse of the linear fit slope in Fig. 10(b).

The dimensionless controller gain $K^* = K\sqrt{h/g}$ is reproduced in Fig. 17(b) at different water levels, for a better understanding of the gain selection.

In order to determine the efficiency and limits of the feedback strategy, an irregular wave train, an undular bore, and regular wave cases were tested. The first example of the implementation of such an absorption strategy for irregular waves is shown in Fig. 18. A wave train is generated by the wavemaker on the left with the help of a smooth velocity pulse function defined as

$$U_G(t) = -\frac{S}{\tau} \operatorname{sech}^2\left(\frac{t-t_0}{\tau}\right), \quad (15)$$

with $S = 0.077$ m, $t_0 = 1.30$ s, and $\tau = 0.342$ s. This function can be visualized in Fig. 3(a). The wave train is moving in the direction of the wave-absorber at the right end part of the wave tank and is formed of a leading trough followed by wiggles (see time $t = 3.5$ s). The waves are then absorbed according to the feedback control strategy with an update of the absorption velocity at every time step, where the error at the wave-absorber wavemaker is plotted in

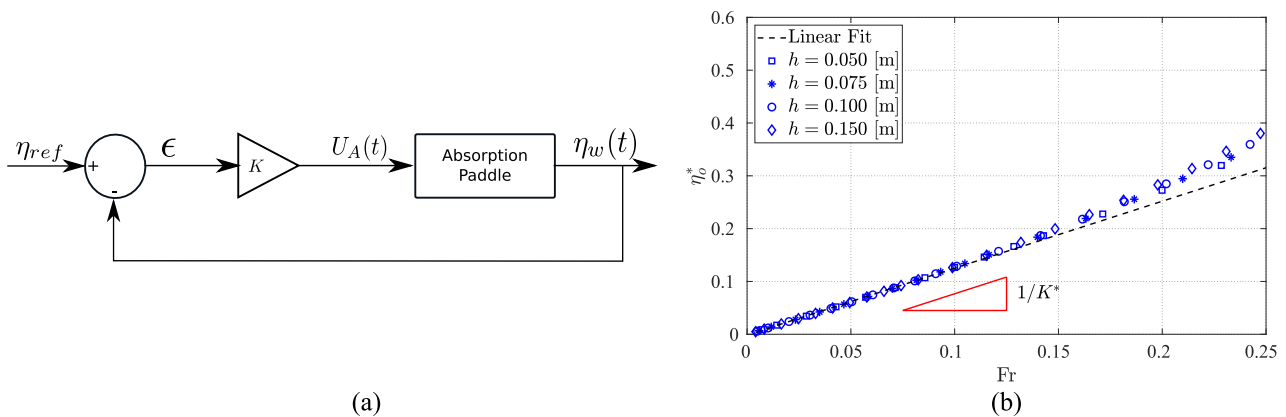


FIG. 17. (a) Absorption block system. A proportional controller compares the value of the water level at the wave-absorber wavemaker η_w with a reference value η_{ref} . It multiplies then the error with a constant coefficient K , which gives the absorption velocity U_A . Error ϵ and absorption velocity as a function of time. (b) Dimensionless overshoot-wave height at the paddle as a function of the Froude number, zoomed-in view of Fig. 10(b). The dimensionless proportional coefficient K^* is represented on the curve as the inverse of the slope (in red). $K^* = 1/1.267$ so that $K = 1/1.267\sqrt{g/h}$.

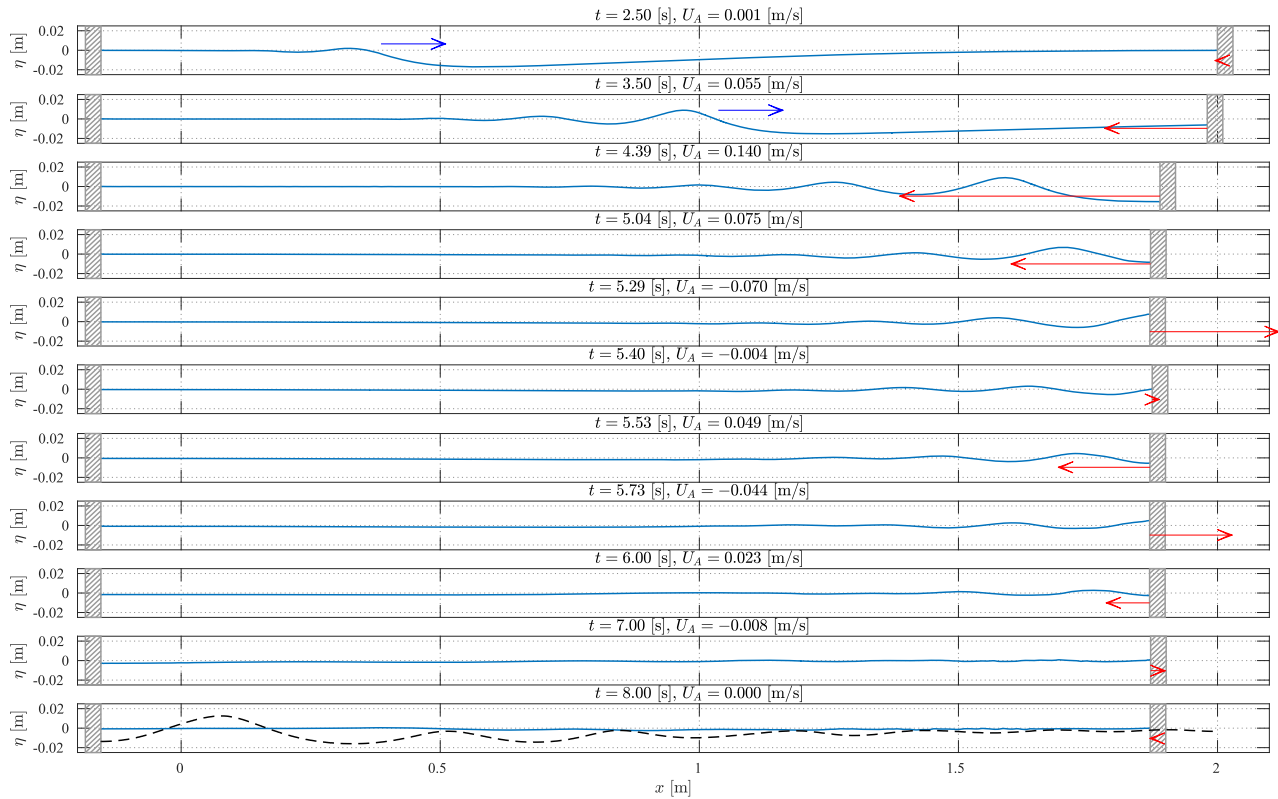


FIG. 18. Wave profile η as a function of the x -coordinate and for times from 2.50 s to 8.00 s. For times $t = 2.20$ s and 3.50 s, a blue arrow indicates the direction of the incident wave train. The active feedback absorber velocity and direction [in the frame of reference (x', z')] are shown with red arrows. For the last time ($t = 8$ s), the wave state for the case without absorption is superimposed in the dashed black line.

Fig. 19(a). The error alternates between positive and negative values causing the absorption velocity U_A , which is also shown in the same graph, to behave similarly. The error decreases to zero while the wave-absorber performs the canceling action. The maximum error corresponds to 21% of the mean water level, that is to say, at the limit of the non-linear portion of the plot in Fig. 10(b). It results in an almost fully absorbed wave state at times $t = 7$ s and 8 s, where the water surface is calm at every location of the wave tank. Note that a reflected wave will take a time greater than $t > 8$ s to arrive into the wave-absorber after reflection at the left wavemaker. That means the error $\varepsilon(t)$ falls to zero rapidly. In Fig. 18, in the last snapshot at $t = 8$ s, the black dashed curve is obtained with the controller off, and thus, the wave-absorber is at rest, allowing one to qualitatively compare the efficiency of the absorption strategy. It is possible to compute the energy of the wave tank in order to evaluate (and propose) the absorption efficiency of our method. The kinetic energy and potential energy per unit width (in J/m) for the water phase are defined as

$$E_c = \frac{1}{2}\rho \int_{X_G}^{X_A} \int_0^{h+\eta} (u_x^2 + u_z^2) dx dz, \quad (16)$$

$$E_p = \rho g \int_{X_G}^{X_A} \int_0^{h+\eta} z dx dz,$$

where u_x and u_z are the horizontal and vertical fluid velocities, respectively. The initial energy (at $t = 0$ s) is equal to the potential energy of the still water level, that is to say, $E_0 = \rho g L h^2 / 2$. As the tank length is not constant in time since both generating and absorbing wavemakers move at positions $X_G(t)$ and $X_A(t)$, a reference energy, which corresponds to the potential energy of the tank for a still water level retrieved by volume conservation considering these new positions, is defined as

$$E_{ref}(t) = \frac{1}{2}\rho g \left(\frac{L^2 h^2}{X_A(t) - X_G(t)} \right). \quad (17)$$

Results of the energy computations are shown in Fig. 19(b), and they are shown with the initial energy state E_0 as a basis. We observe the decrease in the energy in the system during the generation process ($t < 2$ s), then a plateau corresponding to the wave propagation stage ($2 \leq t \leq 3$ s), and finally an increase in the energy (until $t = 8$ s), which is due to the wave absorption of the incident waves and its convergence until a final energy value. We can compare these results with the case without absorption where we observe a nearly constant value of the total energy once the generating wavemaker stops. It is interesting to note the permanent trade between kinetic and potential energies as the waves reflect on the still wavemakers. The slight decrease in total energy is due to wave attenuation during

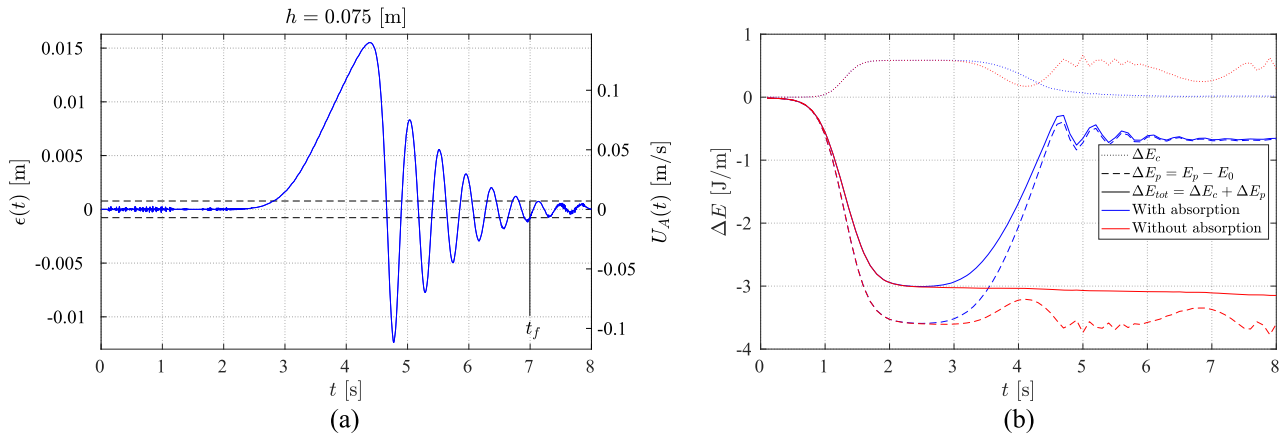


FIG. 19. Case of the absorption of an irregular wave train generated by Eq. (15) for a still water level $h = 0.075$ m. (a) Proportional controller error ε as a function of time. The corresponding velocity of the wave-absorber [in the frame of reference (x', z')] is indicated in the second y axis on the right. The 5% error band is indicated by the black dashed curve, and the corresponding final time $t_f = 7.00$ s is indicated. (b) Energy as a function of time. Kinetic, potential, and total energies are shown with reference to the initial energy in the tank E_0 .

propagation and reflection against the still walls. An estimation of the reflection coefficient can be made by computing the energy ratio between incident and reflected waves (adapted from Ref. 46),

$$C_R = \sqrt{\frac{E_R}{E_I}} = \sqrt{\frac{|E_p(t_f) + E_c(t_f) - E_{ref}(t_f)|}{\max(|E_p(t) + E_c(t) - E_{ref}(t)|)}}, \quad (18)$$

where E_I and E_R are the incident and reflected wave energies and t_f is the time when the error reaches and stays inside 5% of the error band such that $|\varepsilon(t \geq t_f)| \leq \max(|\varepsilon(t)|) \times 5/100$ is verified. The time t_f as well as the 5% error band is indicated in Fig. 19(a). We make sure that at this time, no re-reflection on the absorbing wavemaker has occurred. Perfect wave absorption would lead to $E_{tot} = E_{ref}(t_f)$, but as some reflection happens, this energy level is not reached. It

is important to take into account the reference energy as the length of the wave tank is not constant, thus impacting the general level of potential energy. The computation of the reflection coefficient with this method leads to $C_R = 16\%$. Another analysis is carried out thanks to the separation of incident and reflected wave fields by means of the Fourier transform of two wave gauge data recordings at different tank locations.⁴⁶ It leads to the value of $C_R = 15\%$, which is similar to the previous one and shows the attenuation in the wave absorption process.

The waterfall plot in Fig. 20(a) helps to visualize the motion of the wavemakers as illustrated by the extension of the wave tank at the left during the wave generation and the oscillations of the wave-absorber wavemaker as the incident waves make contact with the wall sensor. Finally, the efficiency of the process can be observed as

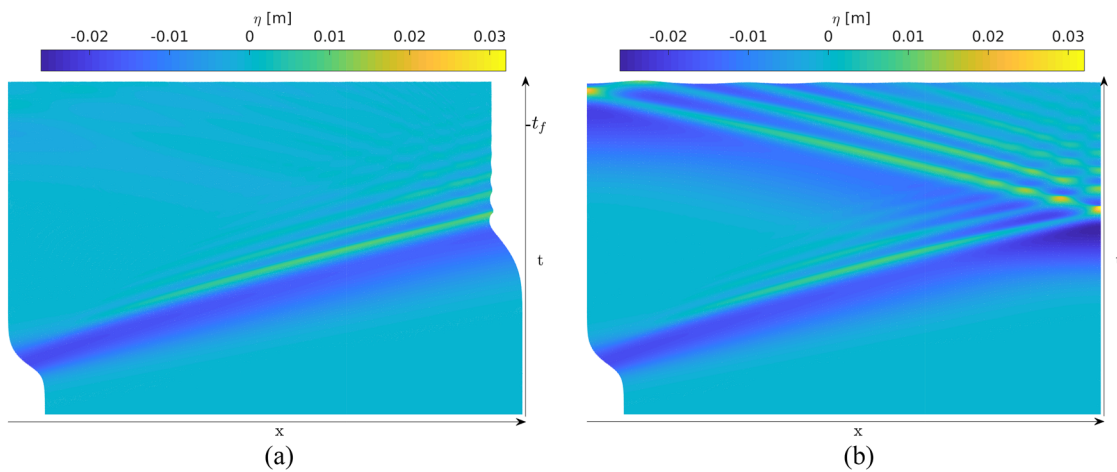


FIG. 20. Waterfall plot of the wave train propagating in the wave tank for a still water level of $h = 0.075$ m. The generating wavemaker follows the velocity defined by Eq. (15). (a) With active absorption. (b) Without active absorption.

the reflected waves are small compared to the initial waves. A comparison with the case without absorption is also plotted in Fig. 20(b) and shows that the wave height at the (still, controller off) wave-absorber wavemaker fully fluctuates between low ($\eta_w < -0.025$ m) and high ($\eta_w > 0.03$ m) values. When the controller is turned on, those fluctuations disappear and $\eta_w \rightarrow 0$ as a result of the absorption mechanism.

The second test case consists in an undular bore, which is generated with a velocity square function defined as

$$U_G(t) = U_0(\Theta(t) - \Theta(t - t_0)), \quad (19)$$

where $U_0 = 0.2$ m/s, $t_0 = 2.5$ s, and Θ is the Heaviside function, for a 4 m long wave tank and a still water level of $h = 0.075$ m. The undular bore, shown in Fig. 21, is generated on the left, propagates toward the wave-absorber wavemaker on the right, and is absorbed according to the proportional strategy. In this case, the error is almost always negative at the wave-absorber wall, with variations due to the incoming bore wiggles, as shown in Fig. 22(a). The starting error is important due to the high amplitude incoming undular bore, but rapidly the controller action decreases it and makes the stationary error converge to zero. In Fig. 22(b), the energy analysis is shown and a similar behavior is observed as in the previous case, with an increase in the total energy during the wave generation and a

constant level during the propagation stage ($0 \text{ s} \leq t \leq 2.5 \text{ s}$ for the first one and $2.5 \text{ s} \leq t \leq 4 \text{ s}$ for the second one).

The total energy then decreases as long as the wave-absorber actuates and converges to the final energy, which corresponds to the final still position of both wavemakers. An estimation of the reflection coefficient can be made with the energy analysis and conducts to $C_R = 10\%$. The analysis of the reflection coefficient in Ref. 46 leads to $C_R = 16\%$. The difference can be explained by the method in Ref. 46, which is not well suited for high amplitude non-linear waves as can be the undular bore. This analysis shows that the strategy is interesting and can effectively absorb non-regular waves, even steep waves.

Finally, tests are carried out on harmonic cases, consisting of the absorption of regular waves generated as for the wave propagation mesh study in Sec. II D 2. The excitation functions and general setups are reported in Table VI. The reflection coefficient is calculated according to Ref. 46 and leads to a value lower than 10% for both cases, showing the efficiency of the proposed strategy in order to absorb waves. A summary of all test cases is reported in Table VI, and the reflection coefficients are given.

When we considered the steady state value of the step response, η_{ss} , it was shown that the water level at the wavemaker reached a constant value after a short time, t_s , at which $\eta_w/h = Fr$, as shown in Fig. 9(b). The absorption velocity and constant coefficient K may be

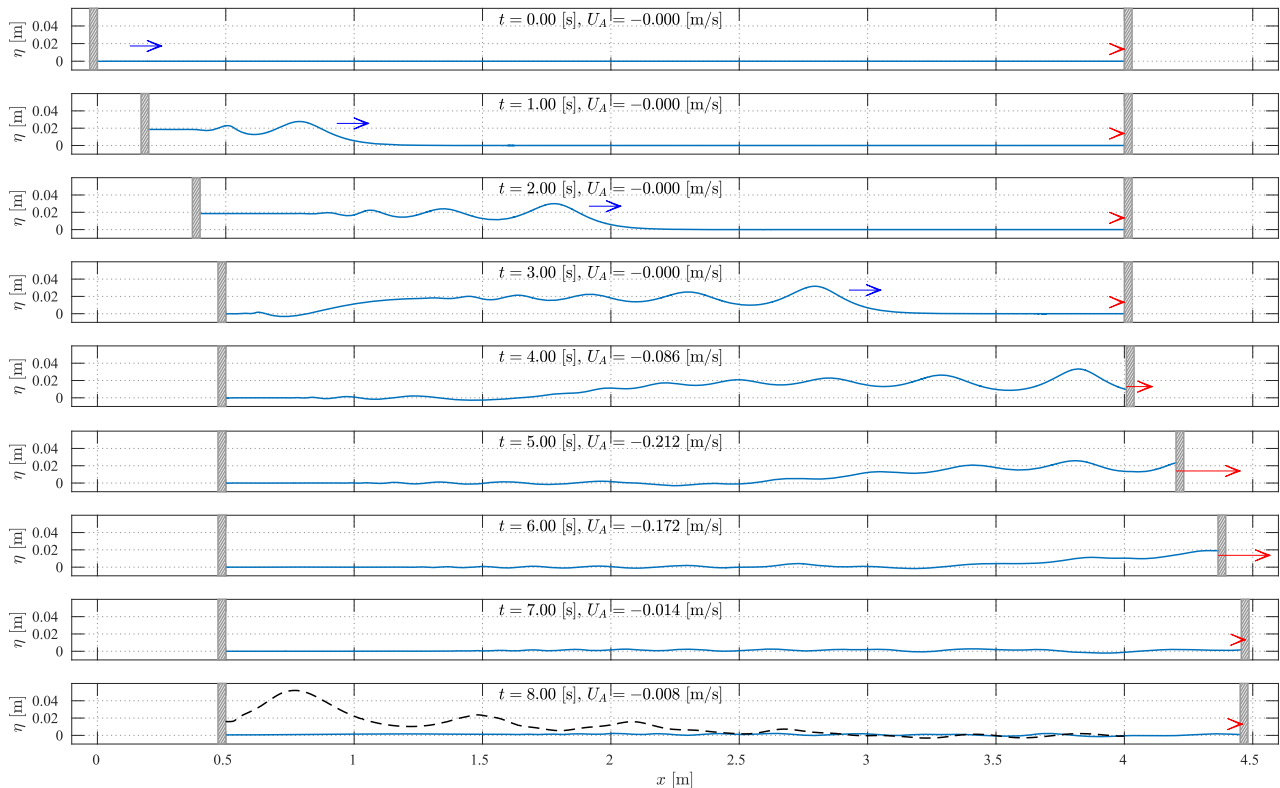


FIG. 21. Wave profile η as a function of the x -coordinate and for times from 0 s to 8.0 s for the undular bore absorption. For times $t = 0$ s and 3 s, a blue arrow indicates the direction of the incident wave train. The active feedback absorber velocity and direction [in the frame of reference (x' , z')] are shown with red arrows. For the last time ($t = 8$ s), the wave state for the case without absorption is superimposed in the dashed black line.

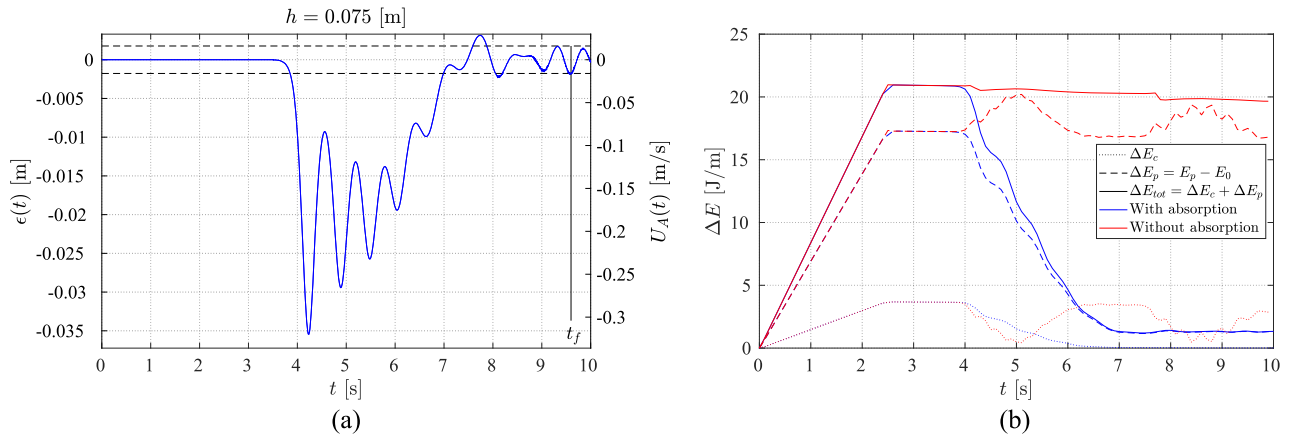


FIG. 22. Case of the absorption of an undular bore generated by Eq. (19) for a still water level $h = 0.075$ m. (a) Proportional controller error ϵ as a function of time. The corresponding velocity of the wave-absorber [in the frame of reference (x', z')] is indicated in the second y axis on the right. The 5% error band is indicated by the black dashed curve, and the corresponding final time $t_f = 9.49$ s is indicated. (b) Energy as a function of time. Kinetic, potential, and total energies are shown with reference to the initial energy in the tank E_0 .

TABLE VI. Test cases for the absorption controller and reflection coefficients.

Wave type	Piston velocity function $U_G(t)$	Parameters	Reflection coefficient C_R	
			Method in Ref. 46 (%)	Energy method (%)
Irregular wave train	$-\frac{S}{\tau} \text{sech}^2\left(\frac{t-t_0}{\tau}\right)$	$h = 0.075$ m, $S = 0.077$ m, $\tau = 0.342$ s, $t_0 = 1.30$ s, $L = 2$ m	15	16
Undular bore	$U_0(\Theta(t) - \Theta(t - t_0))$	$h = 0.075$ m, $U_0 = 0.2$ m/s, $t_0 = 2.5$ s, $L = 4$ m	16	10
Harmonic	$X_0\pi f \sin(2\pi ft + \delta)$	$h = 0.15$ m, $X_0 = 0.004$ m, $f = 1.25$ Hz, $\delta = -\pi/2$, $L = 8$ m	5	...
Harmonic	$X_0\pi f \sin(2\pi ft + \delta)$	$h = 0.05$ m, $X_0 = 0.04$ m, $f = 0.5$ Hz, $\delta = -\pi/2$, $L = 8$ m	9	...

alternatively defined according to $U_A = K\epsilon(t)$ with $K = \sqrt{g/h}$. This coefficient was already given in Ref. 47 and was deduced from a mathematical study of the problem. The choice of the first strategy based on the overshoot ($K = 1/1.267\sqrt{g/h}$) rather than this last one is justified by the peak time t_p associated with the overshoot, which is shorter than the settling time t_s associated with the steady state, as shown in Fig. 11, or better said, the wavemaker moving at constant speed generates a transient wave that is used to cancel the incident wave.

The active wall driven by a feedback controller has proven to be useful not only to cancel wave reflections but also to attenuate high amplitude irregular wave impacts as in the undular bore example. In the future work, we will push further the absorption strategy to effectively reduce the consequences of extreme high amplitude waves using controllers for non-linear waves.

IV. CONCLUSION

In this work, we performed numerical simulations of a two-dimensional wave tank in order to study the piston-type wavemaker

initial-value problem and wave generation using the free and open-source code *OpenFOAM*. The numerical model reproduced the motion of a solid body piston-type wavemaker by moving a solid boundary driven by an external arbitrary signal waveform. We considered a fully viscous model solving the unsteady Navier–Stokes equations on the basis of a two-phase flow strategy and the volume of fluid method to capture the free surface dynamics. Velocity step signals (Heaviside functions) were applied to the piston-type wavemaker, generating a pulse-like wave that propagated along the tank followed by smaller waves or wiggles, which was identified as an undular bore. Recording of the wave elevation time series at the moving wall and in different tank locations was compared with theoretical data, providing a very good agreement and proving the capabilities of the *OpenFOAM* solver *interDyMFoam* to simulate two-phase flows with wave propagation involving both free surfaces and moving boundaries. Wave elevation at the piston wall was found to have close similarity to the time response of the second order system found in feedback theory. In particular, the overshoot and rise, peak, and settling timescales were very close to those in the theory. The scaling found for water elevation at the piston wall at different step

velocities and mean still water levels was in close agreement with that in the theory for low Froude numbers.¹¹ At higher Froude numbers, the scaling differs considerably from that in the theory, being unable to take into account the main wave dynamics. The resulting main wave pulse is generated and detaches from the piston wall at the same time as the overshoot takes place in the wall elevation signal; thus, we call this wave the overshoot-wave. Results along the tank downstream agree with those of potential theory. The overshoot-wave propagates faster than piston velocity increasing its velocity and reaching asymptotically the shallow water celerity downstream the tank. As we solved fully viscous equations, we were able to quantitatively determine the power input during the step response associated with the wave generation process using the entire stress tensor at the piston wall. Net piston forces were obtained integrating pressure and shear stresses on the piston wall. A power scaling was found for different mean still water levels and step velocities as a function of the Froude number.

Finally, in this work, we proposed a feedback proportional controller driving a secondary piston for wave absorption, where the controller gain was determined from the wavemaker step response. The feedback controlled piston method proved to be very efficient on both regular and irregular wave absorption. This novel approach provided the basis from which more complex active wave generation/absorption strategies can be further implemented on numerical and experimental wave tanks to improve efficiency under the influence of different parameters such as the water depth, the wave steepness, and negative velocity steps.

AUTHORS' CONTRIBUTIONS

C.B. and R.H.H. contributed equally to this work.

ACKNOWLEDGMENTS

C.B. wants to thank LEAF-NL for the use of the computing cluster and experimental facilities. This work was funded by National Agency for Research and Development (ANID)/Scholarship Program / Doctorado Nacional/2016–21160553. This research was partially supported by the supercomputing infrastructure of the NLHPC (ECM-02). The authors are also grateful to the Marine Energy Research & Innovation Center (MERIC) and the Mechanical Engineering Department (DIMEC) at Universidad de Chile.

DATA AVAILABILITY

The data that support the findings of this study are available from the corresponding author upon reasonable request.

REFERENCES

- ¹G. Payne, "Guidance for the experimental tank testing of wave energy converters," Supergen Marine technical report, 2008.
- ²B. Holmes, "Tank testing of wave energy conversion systems: Marine renewable energy guides," EMEC technical report, 2009.
- ³T. H. Havelock, *London, Edinburgh Dublin Philos. Mag. J. Sci.* **8**, 569 (1929).
- ⁴F. Biésel and F. Suquet, *Houille Blanche* **6**, 147 (1951).
- ⁵F. Ursell, R. G. Dean, and Y. S. Yu, *J. Fluid Mech.* **7**, 33 (1960).
- ⁶O. S. Madsen, *Coastal Eng. Proc.* **1**, 36 (1970).
- ⁷H. A. Schäffer, *Ocean Eng.* **23**, 47 (1996).
- ⁸D. G. Goring, "Tsunamis—the propagation of long waves onto a shelf," Technical Report 38, 1978.
- ⁹J. Boussinesq, *J. Math. Pures Appl.* **17**, 55 (1872).
- ¹⁰W. M. Lin, J. J. Newman, and D. K. Yue, in *Proceedings of 15th Symposium on Naval Hydrodynamics* (Washington National Academy Press, 1984), pp. 33–49.
- ¹¹S. W. Joo, W. W. Schultz, and A. F. Messiter, *J. Fluid Mech.* **214**, 161 (1990).
- ¹²A. J. Roberts, *Q. J. Mech. Appl. Math.* **40**, 129 (1987).
- ¹³S. W. Joo and M. S. Park, *J. Mech. Sci. Technol.* **20**, 882 (2006).
- ¹⁴M. A. Grosenbaugh and R. W. Yeung, *J. Fluid Mech.* **209**, 57 (1989).
- ¹⁵J. Uddin and D. J. Needham, *J. Fluid Mech.* **776**, 37 (2015).
- ¹⁶C. Song and A. I. Sirviente, *Phys. Fluids* **16**, 2649 (2004).
- ¹⁷H. A. Wolgamot and C. J. Fitzgerald, *Proc. Inst. Mech. Eng., Part A* **229**, 772 (2015).
- ¹⁸P. Higuera, I. J. Losada, and J. L. Lara, *Coastal Eng.* **101**, 35 (2015).
- ¹⁹A. Khaït and L. Shemer, *Phys. Fluids* **30**, 057103 (2018).
- ²⁰C. W. Hirt and B. D. Nichols, *J. Comput. Phys.* **39**, 201 (1981).
- ²¹G. Clauss and C. E. Schmittner *et al.*, in *ASME 2005 24th International Conference on Offshore Mechanics and Arctic Engineering* (American Society of Mechanical Engineers Digital Collection, 2005), pp. 785–792.
- ²²A. Maguire and D. Ingram, in *Eighth European Wave and Tidal Energy Conference (EWTEC, Uppsala, Sweden, 2009)*, pp. 7–10.
- ²³A. Maguire and D. Ingram, in *Proceedings on the Third International Conference of the Application of Physical Modelling to Port and Coastal Protection (COASTLAB, 2010)*, p. 1.
- ²⁴M. A. Bhinder, C. G. Mingham, D. M. Causon, M. T. Rahmati, G. A. Aggidis, and R. V. Chaplin, "A joint numerical and experimental study of a surging point absorbing wave energy converter (WRASPA)," in *Ocean Engineering: Ocean Renewable Energy; Ocean Space Utilisation, Parts A and B* (2009), Vol. 4, pp. 869–875.
- ²⁵P. Higuera, J. L. Lara, and I. J. Losada, *Coastal Eng.* **71**, 102 (2013).
- ²⁶C. Altomare, J. M. Domínguez, A. J. C. Crespo, J. González-Cao, T. Suzuki, M. Gómez-Gesteira, and P. Troch, *Coastal Eng.* **127**, 37 (2017).
- ²⁷D. Liang, W. Jian, S. Shao, R. Chen, and K. Yang, *J. Fluids Struct.* **69**, 72 (2017).
- ²⁸N. S. Nise, *Control System Engineering* (John Wiley & Sons, New York, 2011).
- ²⁹A. E. Maguire, <http://hdl.handle.net/1842/5780>, 2011.
- ³⁰E. Berberović, N. P. Van Hinsberg, S. Jakirlić, I. V. Roisman, and C. Tropea, *Phys. Rev. E: Stat., Nonlinear, Soft Matter Phys.* **79**, 036306 (2009).
- ³¹H. Rusche, "Computational fluid dynamics of dispersed two-phase flows at high phase fractions," Ph.D. thesis, University of London, 2002.
- ³²S. A. Yang and A. T. Chwang, *J. Eng. Mech.* **118**, 735 (1992).
- ³³H. G. Weller, G. Tabor, H. Jasak, and C. Fureby, *Comput. Phys.* **12**, 620 (1998).
- ³⁴S. Patankar, *Numerical Heat Transfer and Fluid Flow* (CRC Press, 1980).
- ³⁵R. I. Issa, *J. Comput. Phys.* **62**, 40 (1986).
- ³⁶I. B. Celik, U. Ghia, P. J. Roache, and C. J. Freitas, *J. Fluids Eng.* **130**, 078001 (2008).
- ³⁷E. Didier, P. R. F. Teixeira, and M. G. Neves, *Defect Diffus. Forum* **372**, 1 (2017).
- ³⁸E. Buckingham, *Phys. Rev.* **4**, 345 (1914).
- ³⁹H. Favre, *Étude théorique et expérimentale des ondes de translation dans les canaux découverts* (Dunod, 1935), Vol. 150.
- ⁴⁰D. H. Peregrine, *J. Fluid Mech.* **25**, 321 (1966).
- ⁴¹J. J. Stoker, *Water Waves: The Mathematical Theory with Applications* (Wiley-Interscience, 1957), p. 328.
- ⁴²S. D. Hatland and H. Kalish, *Phys. Fluids* **31**, 033601 (2019).
- ⁴³P. A. Madsen, D. R. Fuhrman, and H. A. Schäffer, *J. Geophys. Res.: Oceans* **113**, C12012 (2008).
- ⁴⁴D. Ingram, R. Wallace, A. Robinson, and I. Bryden, in *Proceedings of Oceans 2014 MTS/IEEE* (Institute of Electrical and Electronics Engineers, IEEE, Taipei, Taiwan, USA, 2014).
- ⁴⁵J. P. McHugh and D. W. Watt, *Phys. Fluids* **10**, 324 (1998).
- ⁴⁶Y. Goda and Y. Suzuki, "Estimation of incident and reflected waves in random wave experiments," *Coastal Eng.* **1**(15), 47 (1976).
- ⁴⁷H. A. Schäffer and K. Jakobsen, "Non-linear wave generation and active absorption in wave flumes," in *Long Waves Symposium, Thessaloniki, Greece, 2003*.